The Pennsylvania State University
The Graduate School
College of Earth and Mineral Sciences

FORMATION OF ARCTIC STRATOCUMULUS CLOUDS IN ADVECTING AIR MASSES

A Thesis in
Meteorology

by
Lucien F. Simpfendoerfer

Submitted in Partial Fulfillment
of the Requirements
for the Degree of
Master of Science

August 2018

The thesis of Lucien Simpfendoerfer was reviewed and approved* by the following:

Johannes Verlinde
Professor of Meteorology and Atmospheric Science
Associate Head, Graduate Program in Meteorology and Atmospheric Science
Thesis Advisor

Jerry Y. Harrington
Professor of Meteorology

Eugene E. Clothiaux
Professor of Meteorology and Atmospheric Science

Matthew Shupe
Research Scientist, Cooperative Institute for Research in Environmental Sciences at the University of Colorado and the NOAA Earth System Research Laboratory
Special Signatory

*Signatures are on file in the Graduate School

ABSTRACT

Remote sensing observations across the Arctic indicate that Arctic stratocumuli must form through the cooling of advecting air masses during all seasons, not only in summer as was previously proposed. In this study, radiative transfer calculations and single column model simulations are used to investigate Arctic stratocumuli formation processes and their sensitivities. First, a radiative transfer model and clear-sky radiosonde observations from near Barrow, Alaska, are used to learn about the processes that drive and inhibit cooling within advecting air masses in the Arctic. Next, a single column model simulation is used to investigate how Arctic stratocumuli form when ice precipitation is involved in the formation process. Finally, sets of single column simulations are used to investigate formation processes' sensitivities to the availability of moisture, the background static stability, and the ice precipitation rate.

Radiative transfer calculations show that Arctic stratocumuli may form through radiative cooling and/or synoptic-scale lifting, and that subsidence is more effective than solar heating in inhibiting cloud formation. The single column model simulations show that ice inhibits the growth of liquid during the formation process and that the outcome of the formation process is extremely sensitive to the environment in which the process occurs. Arctic stratocumuli that form in moist environments with low concentrations of ice forming nuclei are likely to become optically thick and exert a large radiative forcing on the surface. Conversely, Arctic stratocumuli that form in dry environments or in environments with high concentrations of ice forming nuclei are likely to become optically thin or dissipate and exert a small radiative forcing on the surface. Static stability affects the formation process by modifying entrainment rates and therefore modifying the processes' sensitivities to the availability of moisture above and below. The results highlight the importance of precipitation-radiative-dynamical interactions in simulating Arctic stratocumuli in larger-scale models.

TABLE OF CONTENTS

LIST OF FIGURES

LIST OF TABLES

ACKNOWLEDGEMENTS

Thank you to my thesis supervisor, Dr. Johannes Verlinde, and my committee members, Dr. Jerry Harrington, Dr. Eugene Clothaiux, and Dr. Matthew Shupe, for your invaluable guidance and input. Thank you especially to Dr. Johannes Verlinde for your academic advice and encouragement over the past five years. I am absolutely convinced I would not have earned the dual BS/MS, made it to Svalbard, or done nearly as well as I did without you. Thank you also to Karen Corl for all of the help you provided in navigating complex administrative procedures. Finally, an enormous thanks to Claudia, Thomas, Leila, and Sage for your support and encouragement throughout this long and difficult endeavor. This research was supported by the U.S. Department of Energy's Atmospheric Science Program Atmospheric System Research, an Office of Science, Office of Biological and Environmental Research program, under Grant DE-SC0013953.

Chapter 1

Introduction

Arctic surface temperatures are increasing more than twice as rapidly as in the mid-latitudes through a process known as Arctic amplification (Overland et al. 2014). Arctic amplification is disrupting Arctic terrestrial, freshwater, and marine ecosystems at rates that may outpace the ecosystems' abilities to adapt, and is threatening food security and ways of life in indigenous and other communities across the Arctic (Larsen et al. 2014). Arctic amplification is also relaxing the equator-to-pole temperature gradient, which may change mid-latitude storm tracks, slow the progression of mid-latitude weather patterns, and consequently alter mid-latitude climate (Cohen et al. 2014). Recent studies have shown that an increase in downwelling longwave radiation is a primary cause of Arctic amplification in winter (Gong et al. 2017; Lee et al. 2017).

Clouds are a primary contributor to downwelling longwave radiation in the Arctic. Across the Arctic, the distribution of the net longwave (NetLW) irradiance at the surface is bimodal in winter (Figure 1-1). The lower NetLW peak corresponds to periods of clear skies, while the higher peak corresponds to periods of cloudy skies (Stramler et al. 2011). When skies are clear, surface temperatures plunge because the surface rapidly loses energy that is not replenished through the exchange of longwave radiation with the atmosphere. When skies are cloudy, the surface temperature remains warm because the surface gains energy through the exchange of longwave radiation with the atmosphere (Intrieri et al. 2002; Stramler et al. 2011; Morrison et al. 2011a). Therefore, to understand and predict Arctic amplification, scientists must understand the processes that lead to the formation, persistence, and dissipation of each type of cloud in the Arctic.

One dominant species of cloud in the Arctic is stratocumulus. Arctic stratocumuli may be composed of only liquid or a mixture of liquid and ice. They are typically neutrally stratified, and exist within turbulent mixed layers that are either dynamically coupled or decoupled from the surface (Curry et al. 1988; Shupe et al. 2013; Sotriopoulou et al. 2014). Arctic stratocumuli play a key role in the Arctic climate because they are often optically thick in both the longwave and the shortwave and exist in broad sheets that may persist from several hours to several days (Curry et al. 1988; Intrieri et al. 2002; Morrison et al. 2011a; Shupe et al. 2011; Sotriopoulou et al. 2014). For these reasons, they have also been the subject of extensive study. However, a majority of studies have focused on the processes that allow the cloud layers to persist for long periods of time. Relatively little has focused on their formation mechanisms.

Thus far, several formation mechanisms have been proposed. First, they can form as stratocumuli form in subtropical environments: through the growth of atmospheric boundary layers that are maintained through surface fluxes (Harrington and Olsson 2001; Klein et al. 2009; Wood 2012). While this is a dominant formation mechanism over the open ocean during cold air outbreaks, it does not appear to be a dominant formation mechanism over pack ice or land, where surface fluxes are typically smaller (Persson et al. 2002). Second, Arctic stratocumuli may form from surface-based radiation fogs. If a surface fog forms under clear skies and becomes optically thick, radiative cooling of fog droplets becomes increasingly concentrated near cloud top, which destabilizes the fog layer and generates a turbulent mixed layer. Entrainment from above by this mixed layer allows the fog to gradually lift and transform into an elevated Arctic stratocumulus cloud layer (Herman and Goody 1976; Houze 2014; Tjernström et al. 2015). This was initially proposed as a formation mechanism for summertime Arctic stratocumuli, but simulations suggest that mixed-phase stratocumuli may also form by this mechanism over pack ice in winter (Curry 1983; Pithan et al. 2014; Cronin and Tziperman 2016; Cronin et al. 2017). Finally, Arctic stratocumuli may form through the cooling of air masses that advect across the Arctic. If

processes such as radiative cooling and synoptic scale lifting cool a layer of the atmosphere to liquid saturation, vapor condenses and forms a very tenuous cloud layer (Herman and Goody 1976; McInnes and Curry 1995; Zhang 1999; Garrett et al. 2009). This layer then rapidly deepens through a positive feedback between radiative cooling and condensation (Zhang 2009; Garrett et al. 2009), until it evolves into an elevated Arctic stratocumulus cloud. Thus far, this has only been formally investigated as a formation mechanism in summer.

In this thesis, the formation of Arctic stratocumuli through the cooling of advecting air masses is investigated in more detail. First, clear-sky radiosonde observations from near Barrow, Alaska, and a radiative transfer model are used to provide insight into the cooling processes that lead to the formation of Arctic stratocumuli. Next, a single column model (SCM) is used to determine how ice precipitation affects the formation processes. Finally, the SCM is used to test sensitivities of the formation process to environmental factors such as the background static stability and the availability of moisture.

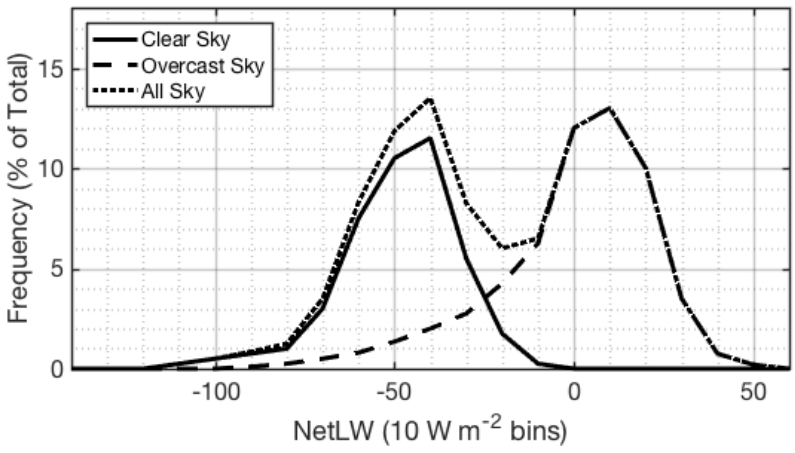

Figure **1-1**. Distributions of the net longwave (NetLW) irradiance at the surface, compiled over the entire Arctic during January 1998. One distribution consists of points under clear skies, another consists of points under cloudy skies, and a third consists of all points regardless of cloudiness. NetLW irradiances were calculated using data from the International Satellite Cloud Climatology Project (ISCPP; Rossow and Schiffer 1999). Figure is modified from Stramler et al. (2011), Figure 10.

Chapter 2

Cooling of advecting air masses

Several modeling studies have suggested that cooling of advecting air masses may lead to the formation of elevated, liquid-only Arctic stratocumuli during summer (Herman and Goody 1976; McInnes and Curry 1995; Zhang 1999; Garrett et al. 2009). Remote sensing observations across the Arctic suggest that the cooling of advecting air masses must drive the formation of Arctic stratocumuli during other seasons and under conditions that allow the production of ice. At remote sensing observatories across the Arctic, cloud layers containing only liquid or a mixture of liquid and ice are routinely present up to 8000 m during summer and up to 4000 m during winter (Shupe 2011). Many of these cloud layers exist too far above the surface to have formed through the lifting of radiation fogs. Instead, they must have formed by a local cooling process, such as synoptic-scale lifting or clear-sky radiative cooling.

Thus far, no statistical context regarding the effectiveness of radiative cooling and synoptic-scale lifting in driving cloud formation throughout the year has been provided. In this chapter, such context is provided using clear-sky radiosonde profiles from the Department of Energy (DOE) Atmospheric Radiation Measurement (ARM) Program observatory near Barrow, Alaska, and a radiative transfer model. The profiles and radiative transfer calculations are also used to discuss the effectiveness of local heating processes in inhibiting cloud formation by local cooling and to constrain sensitivity studies presented in the next chapter of this thesis.

Identification of clear-sky profiles

The DOE ARM Program observatory at the North Slope of Alaska is located near Barrow, AK (71.323ºN, 156.609ºW), and is home to a large suite of atmospheric in situ and remote sensing instruments. In this study, observations from a Ka-band ARM zenith pointing radar (KAZR) and a micropulse lidar (MPL) are used to identify radiosondes that were launched from the NSA observatory between Jan. 1, 2012, and Dec. 31, 2015, during periods of clear skies. Radiosondes are typically launched daily from the NSA observatory at 5:30 UTC and 17:30 UTC and measure vertical profiles of temperature, pressure, and relative humidity up to approximately 20 km. The KAZR (frequency = 35 GHz) measures vertical profiles of reflectivity, Doppler velocity, and spectrum width to an altitude of 20 km, and is effective in detecting most plumes of ice precipitation. However, the KAZR is often too insensitive to small hydrometeors to identify ice-free layers of liquid droplets and tenuous plumes of ice precipitation. The MPL (wavelength = 532 nm) measures vertical profiles of backscattering by aerosols, liquid condensate, and ice condensate to an altitude of 18 km. The MPL is more sensitive than the KAZR to small hydrometeors and is therefore able to detect liquid layers and tenuous plumes of ice precipitation that the KAZR fails to identify. However, the MPL is often unable to observe the atmosphere to high altitudes because its signal rapidly attenuates in optically thick liquid layers and plumes of ice precipitation.

KAZR signal-to-noise ratios (SNRs) and an MPL cloud mask product (Wang and Sassen 2001) were used to identify plumes of ice precipitation and liquid layers between 250 m and 13000 m around the time of each radiosonde launch. The KAZR SNRs were first used to detect plumes of ice precipitation, and the MPL cloud mask was then used to detect smaller ice crystals and liquid droplets that the KAZR may have missed. KAZR and MPL observations within fifteen minutes of the radiosonde launch below 4000 m, thirty minutes of the radiosonde launch between

4000 m and 8000 m, and sixty minutes of the launch above 8000 m were used in the search for hydrometeors. If no plumes of ice precipitation or liquid layers were detected in those observations, the radiosonde was assumed to have encountered only air without hydrometeors in its ascent, and its profile was included in the radiative transfer calculations. These long time windows provide a large sample of the atmospheric conditions above the NSA observatory at the time of each launch, and minimize the probability that each radiosonde encountered undetected hydrometeors during its passage through the atmosphere. The search for hydrometeors was limited to observations above 250 m to increase the sample size of radiosonde observations used to examine cloud formation: hydrometeors below 250 m are unlikely to severely affect radiative heating rates above, except perhaps in cases when opaque fogs form within strong surface-based temperature inversions. The search was also limited to observations below 13000 m because liquid and ice above the NSA observatory were only observed below 13000 m between March 2004 and February 2006 (Shupe 2011). Cases in which the MPL signal attenuates below 250 m were excluded from the analysis.

The method for identifying clear-sky radiosonde launches was verified manually using observations from the High Spectral Resolution Lidar (HSRL) at the NSA observatory, which observes the same sections of the atmosphere as the KAZR and MPL, but is slightly more sensitive than the MPL. Seventy-five cases in which no hydrometeors were detected by either instrument, thirty cases in which hydrometeors were detected by both instruments, and twenty cases in which hydrometeors were detected by the MPL but not by the KAZR were randomly selected for verification. Of the 125 verified cases, only five were classified incorrectly. Each of the five misclassified cases contained plumes of ice crystals above 8000 m. Each of these plumes produced HSRL backscatter that was only slightly larger than the backscatter produced by typical aerosol layers, and were therefore most likely too tenuous to significantly affect heating rates elsewhere in the profile. The verification indicates that the methodology performs very well in

identifying clear-sky radiosonde launches, and that the decision to use the MPL instead of the more sensitive HSRL to identify clear-sky launches is of little consequence.

In all, 418 of the 3369 radiosondes launched at the NSA site between Jan. 1, 2012, and Dec. 31, 2015, are likely to have observed profiles free from hydrometeors. 51% of these clear-sky launches occurred in winter (Dec-Mar), 16% in spring (Apr-May), 21% in summer (Jun-Aug), and 12% in autumn (Sept-Nov).

Simulation of radiative cooling

Each of the clear-sky radiosonde profiles was cooled to saturation using iterative longwave and shortwave radiative transfer calculations performed with the Rapid Radiative Transfer Model (RRTM; Mlawer et al. 1997; Mlawer and Clough 1997). These iterative calculations were initialized with profiles of temperature (T), water vapor mixing ratio (r_v), and pressure (p) measured by a radiosonde. Because radiosonde measurements do not extend to the top of the atmosphere, the radiosonde profiles of p, T, and r_v were supplemented between 20 km and 68 km by values from the default sub-Arctic winter sounding provided by RRTM. To ensure that discontinuities do not exist where the radiosonde profiles are joined with the default soundings, the profiles of T and r_v were interpolated linearly from the radiosonde observation closest to 18 km to the default sub-Arctic winter sounding values at 20 km. The profile of CO_2 was assumed to be well mixed with a uniform concentration of 400 ppm, while the profiles of O_3, N_2O, CH_4, O_2, and CO were initialized with values from the RRTM default sub-Arctic winter sounding. No liquid or ice condensate was included in the radiative transfer calculations. Although aerosol particles do influence radiative transfer in the Arctic atmosphere, they were excluded from these calculations to isolate the role thermodynamic profiles play in the clear-sky radiative cooling process.

The iterative radiative transfer calculations were performed with a time step of sixty minutes for a total of five days or until the clear-sky profile saturated above 250 m (lowest height checked for hydrometeors with the KAZR and MPL). Longwave calculations were performed at four angles (8 streams), and at vertical resolutions of 25 m below 5000 m, 200 m between 5000 m and 20000 m, and 2000 m above 20000 m. Shortwave calculations were performed at vertical resolutions of 50 m below 5000 m, 200 m between 5000 m and 20000 m, and 2000 m above 20000 m. At the beginning of each time step, the solar zenith angle was updated using ephemeris calculations (Wilson 1980) for the NSA observatory and the surface temperature was reset to the temperature in the lowest atmospheric grid box. After each radiative transfer calculation, temperature profiles were updated using the heating rate profiles output by RRTM and static instabilities were removed using a simple dry-air convective adjustment scheme. Sensitivity tests indicate that the evolution of profiles cooled with the radiative transfer model was insensitive to increases in the vertical or temporal resolution of the radiative transfer calculations.

Results and discussion of radiative transfer calculations

The radiative cooling process for two clear-sky atmospheric profiles observed by radiosonde at the NSA observatory is illustrated in Figure 2-1. The initial temperature profile, the initial dew point profiles, the temperature profiles at various times during the cooling process, and the final temperature profiles are plotted for both launches. The profile in Figure 2-1a exhibits a surface-based temperature inversion of over 10 K and a very variable dew point profile. After forty-two hours of cooling, the profile saturates at 1450 m, which lies near the maxima in the initial profiles of temperature and dew point, and a local minimum in the initial profile of dew point depression. The dew point depressions just above and below the initial point of saturation both exceed 12 K, indicating that the atmosphere is very dry in those regions. The profile in

Figure 2-1b exhibits a weaker surface-based temperature inversion and less variable dew point profile. After twenty-eight hours of cooling, the profile saturates at approximately 675 m, which lies near peaks in both the initial temperature and dew point profiles, and near a local minimum in the initial dew point depression profile. The atmosphere just above and below the initial point of saturation is much moister than in the profile shown in Figure 2-1a, with larger dew points and smaller dew point depressions.

The radiative transfer calculations indicate that both radiative cooling and synoptic scale lifting are capable of producing Arctic stratocumuli during all seasons. Of the 418 clear-sky launches between 2012 and 2015, 20% saturated within twenty-four hours, 47% saturated within forty-eight hours, and 86% saturated within five days when heated/cooled through both longwave and shortwave radiative transfer alone (Figure 2-2a). If a typical uniform vertical velocity of 5.5 mm s^{-1} were imposed on each clear-sky radiosonde profile (Stepanyuk et al. 2017), the dry adiabatic lapse rate dictates that the profiles would cool at rates of approximately 4.7 K day^{-1} through adiabatic expansion. This cooling rate is faster than the average radiative cooling rate at the initial point of saturation in all but one of the profiles. Using a dispersion model, Stohl (2006) found that parcels routinely spend more than five days in the Arctic before exiting. Parcels at higher altitudes often remain in the Arctic for shorter periods, while parcels at lower altitudes typically remain for much longer. Therefore, many of the cloud-free parcels sampled by radiosondes launched from the NSA observatory likely cooled to liquid saturation through radiation, synoptic-scale lifting, or a combination of both before they left the Arctic.

The distribution of heights at which each clear-sky profile saturates is shown in Figure 2-2b. Interestingly, the distribution's shape strikingly resembles that of the vertical distribution of liquid-containing cloud fraction observed at Barrow between 2004 and 2006 (Shupe 2011). Both distributions peak near the surface and decline exponentially with height above 1000 m. If radiosonde profiles that saturate at temperatures below -40 ºC are neglected (liquid clouds cannot

form if cloud droplets freeze rapidly by homogeneous ice nucleation), both distributions also only extend to 7500 m. This implies that if all clear-sky profiles observed by radiosonde at Barrow between 2012 and 2015 cooled over five days, and that if all liquid clouds that formed during that period persisted for the same length of time, the shape of the resulting distribution of liquid-containing cloud fraction would be very similar to that of the distribution observed by Shupe (2011). While this does not necessarily mean that all liquid-containing clouds within Shupe's distributions formed by the cooling of advecting air masses, it does imply that it is possible that many did: the resulting distribution of cloud fraction could be consistent with the observed climatology.

The clear-sky radiative transfer calculations indicate that shortwave heating offsets radiative cooling inconsistently. Figure 2-2c shows the distribution of the average cooling rate from the time of the radiosonde launch to the time of saturation at the initial height of saturation in each profile, while Figure 2-2d shows the fraction of longwave cooling that is offset by shortwave heating at that height in each profile. In 52% of the profiles that saturated within five days, shortwave heating offset less than 5% of radiative cooling. These were all observed during late autumn, winter, and early spring, when very little direct solar radiation is present. In the other 48% of profiles, shortwave heating offset up to 70% (Figure 2-2d). Predictably, these profiles mostly occurred during late spring, summer, and early fall, when solar zenith angles are relatively small at the NSA observatory.

Subsidence is more consistently effective in preventing cloud formation in advecting air masses. If a subsidence velocity of 5.5 mm s^{-1} were imposed, the dry adiabatic lapse rate dictates that adiabatic warming would completely offset radiative cooling in all but one of the profiles. If a subsidence velocity of only 1.5 mm s^{-1} were imposed, adiabatic warming would prevent radiative cooling in 50% and slow cooling in the rest (Figure 2-2c). Both of these subsidence

rates are typical in the Arctic atmosphere (Klein et al. 2009; Morrison et al. 2011b; Ovchinnikov et al. 2014; Stepanyuk et al. 2017).

Inclusion of aerosols in radiative transfer calculations would likely affect the results. Because many moist air masses that advect across the Arctic originate from the mid-latitudes (Devasthale et al. 2011), aerosols are likely to be involved in the cooling process. Dry aerosols in the Arctic are capable of both scattering and absorbing shortwave radiation, but are too small to interact with longwave radiation (Curry 1995). In the summer, these aerosols may slow cloud formation by enhancing the shortwave heating of cloud layers. However, estimates of dry aerosol contributions to heating rates are typically below 1 K day^{-1} (Shaw and Stamnes 1980; Valero and Ackerman 1986). Wet aerosols, or aerosols that have undergone deliquescence, are capable of absorbing and scattering shortwave radiation, and of absorbing and emitting longwave radiation (Curry 1995). Therefore, the presence of wet aerosols is likely to accelerate cloud formation in advecting air masses during winter. In summer, the overall effect of wet aerosols is less certain, and likely depends on the aerosols' specific optical properties and the solar zenith angle.

The radiative transfer calculations provide estimates of the distributions of static stability and moisture availability around the initial point of saturation in each profile. Static stability is estimated by calculating the average vertical temperature gradient from 200 m below the initial point of saturation to 200 m above (Figure 2-2e). Moisture availability above is estimated using the average relative humidity from 200-500 m above the initial point of saturation (RH_{25a}), and moisture availability below is estimated using the equivalent relative humidity below (RH_{25b}). The vertical temperature gradients vary between -9.8 K km^{-1} and 30.0 K km^{-1} in all but one of the profiles (Figure 2-2e). RH_{25a} varies from 7% to 97%, while RH_{25b} varies from 12% to 100% (Figure 2-2f). While these distributions may not be identical to distributions around Arctic stratocumuli when they form in the Arctic atmosphere, they provide estimates for the relevant

ranges of each quantity. These ranges are used to constrain sensitivity studies presented in the next chapter of this thesis.

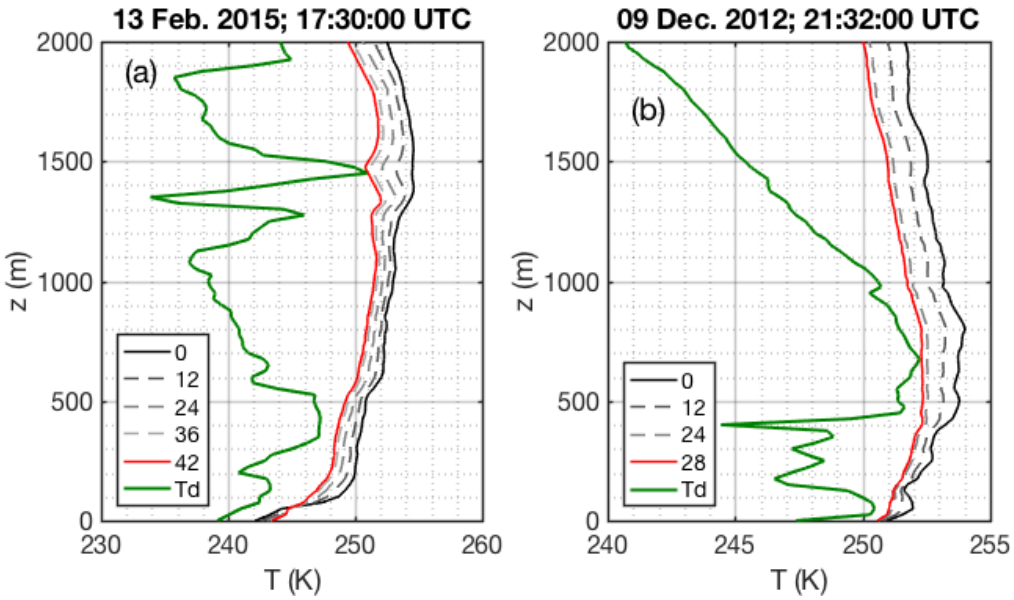

Figure **2-1**: Illustrations of the clear-sky radiative cooling process for atmospheric profiles observed by radiosondes launched from the NSA observatory at (a) 17:30 UTC on Feb. 13, 2015 and (b) 21:32 UTC on Dec. 09, 2012. The solid black lines show the initial temperature profiles, while the green lines show the initial dew point profiles. The dashed lines show profiles of temperature at twelve-hour intervals of cooling (hours of cooling shown in the legend). The solid red line shows the temperature profile when the atmosphere reaches liquid saturation (number of hours required to saturate is shown in the legend).

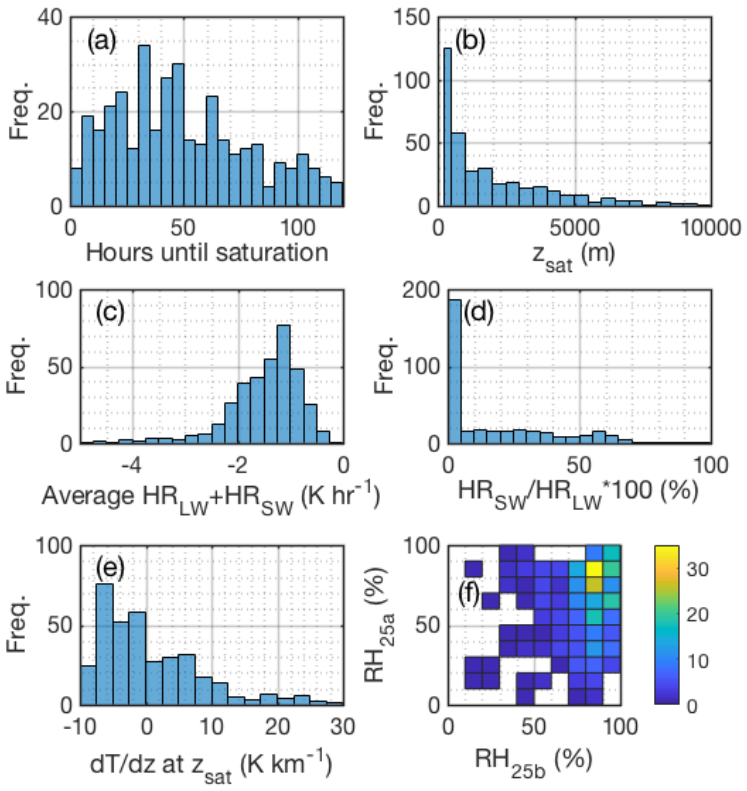

Figure **2-2**: Frequency of occurrence distributions of (a) time required for each clear-sky sounding to saturate, (b) height at which each clear-sky sounding saturates, (c) average total heating rate at the height of saturation, (d) fraction of longwave cooling offset by shortwave heating, and (e) average vertical temperature gradient at the height of cloud formation. (f) Two-dimensional histogram of the average relative humidity from 200-500 m above and below the point in the profile that saturates first, at the time of saturation (RH_{25a} and RH_{25b}, respectively).

Chapter 3

Investigation of formation processes using a single column model

In this chapter, a SCM is used to investigate the formation of Arctic stratocumulus through radiative cooling of advecting air masses when in-cloud temperatures are below freezing and the cloud precipitates ice. The model is also used to investigate how variations in the relative humidity above, relative humidity below, and static stability affect the formation process. A SCM is used in place of large eddy simulations because a comprehensive set of sensitivity tests must cover a broad parameter space, which would be impossible to cover using more computationally expensive large eddy simulations. However, this decision comes at an expense: the SCM cannot resolve turbulent motions or horizontal variability, and is therefore unable to represent breakup of cloud layers or transitions to cumulus regimes. Due to the simplicity of the SCM simulations, analysis of the simulations will focus on first-order interactions between the four basic processes that affect the evolution of neutrally stratified Arctic stratocumuli (radiation, entrainment, precipitation, and subsidence), which the SCM and its parameterizations are able to capture.

Model description

A complete description of the single column model is provided by Golaz (1997). Only a brief overview of the model and of adjustments that were made to the model for the purposes of this study is provided here.

The model is based on the prediction of four prognostic variables: the horizontal wind velocity components (u and v), the ice-liquid potential temperature (θ_{il}), and the total water mixing ratio (r_t). These variables are predicted through four equations:

$$\frac{\partial \overline{u}}{\partial t} = -\overline{w}\frac{\partial \overline{u}}{\partial z} + f\left(\overline{v} - v_g\right) - \frac{\partial \overline{w'u'}}{\partial z} \qquad (1)$$

$$\frac{\partial \overline{v}}{\partial t} = -\overline{w}\frac{\partial \overline{v}}{\partial z} - f\left(\overline{u} - u_g\right) - \frac{\partial \overline{w'v'}}{\partial z} \qquad (2)$$

$$\frac{\partial \overline{\theta_{il}}}{\partial t} = -\overline{w}\frac{\partial \overline{\theta_{il}}}{\partial z} - \frac{\partial \overline{w'\theta_{il}'}}{\partial z} + \left.\frac{\partial \overline{\theta_{il}}}{\partial t}\right|_{\text{rad}} + \left.\frac{\partial \overline{\theta_{il}}}{\partial t}\right|_{\text{sedim}} \qquad (3)$$

$$\frac{\partial \overline{r_t}}{\partial t} = -\overline{w}\frac{\partial \overline{r_t}}{\partial z} - \frac{\partial \overline{w'r_t'}}{\partial z} + \left.\frac{\partial \overline{r_t}}{\partial t}\right|_{\text{sedim}}, \qquad (4)$$

where u_g and v_g represent the west-east and south-north components of the geostrophic wind velocity, w is the vertical velocity, the subscript "rad" indicates a tendency due to radiation, and the subscript "sedim" represents a tendency due to sedimentation. Quantities with over bars signify Reynolds averaged quantities, while quantities with primes signify turbulent fluctuations.

Turbulence and turbulent fluxes are calculated following the 1.5-order turbulence closure scheme described in Bechtold et al. (1992) but with a few modifications. First, the eddy transfer coefficients for the momentum (K_m) and thermodynamic (K_h) variables are related through a ratio $\alpha = \frac{K_h}{K_m}$, where α is computed following Langland and Liu (1996). Second, the mixing and dissipation length scales are assumed to be equal and are computed as the square root of the product of two natural length scales. These natural length scales are computed as in Bechtold et al. (1992). Finally, the buoyancy flux is diagnosed from the vertical fluxes of θ_{il} and r_t if no condensate is present (Golaz 1997, Eq. 2.97), and from the vertical fluxes of θ_{il}, r_t, and the total ice mixing ratio (r_i) if condensate is present (Golaz 1997, Eq. 2.105).

The microphysical parameterization is based on the RAMS single-moment bulk microphysics scheme (Walko et al. 1995), which subdivides r_t into mixing ratios of water vapor, cloud water (r_{cld}), rain (r_r), pristine ice (r_p), snow (r_s), aggregates (r_a), graupel (r_g), and hail (r_h). However, the treatment of pristine ice is replaced with a particle property scheme. The dimensions, growth rates, and fall speeds of pristine ice crystals are predicted using the bulk adaptive habit model, which is described in detail in Harrington et al. (2013). The adaptive habit

model allows the aspect ratios of pristine ice crystals to evolve as the pristine ice crystals grow in environments with different temperatures, and therefore allows a more realistic representation of depositional growth feedbacks. In addition, a new ice nucleation scheme based on the schemes used by Morrison et al. (2011b), Solomon et al. (2014), and Ovchinnikov et al. (2014) is implemented. The scheme only allows ice particles to nucleate in a grid box if r_{cld} > 0.005 g kg^{-1} and if the number concentration of pristine ice crystals is below a certain threshold, N_{ice}. This holds the ice number concentration within the simulated cloud layers effectively constant at N_{ice} and provides a simple means of varying the precipitation rate.

Irradiances are computed using a two-stream radiative transfer model, which is fully coupled to the model microphysics. A complete description of the radiative transfer code can be found in Harrington (1997). The surface is treated as a uniform slab with heat capacity set to 2.1x10^{4} J m^{-2} K^{-1}. The temperature of the slab responds to surface radiative, sensible heat, and latent heat fluxes with an e-folding timescale of 1.5 hours. Surface momentum fluxes are calculated using a surface roughness length of 1x10^{-4} m, which is a typical value for sea ice (Stull 1988).

The model predictive equations are discretized and integrated forward using a Crank-Nicolson type semi-implicit scheme.

Model initialization

The profiles used to initialize all SCM simulations follow a consistent format, shown in Figure 3-1. The temperature profile contains a surface-based temperature inversion, which is likely to develop under clear sky conditions. Between 600 m and 1300 m, the vertical temperature gradient is set to a constant value of dT/dz. Above 1300 m, the temperature decreases with height. The relative humidity decreases quadratically from a peak of 100% at 1000 m to specified values

RH_{bel} at 800 m and RH_{abv} at 1200 m. Below 800 m and above 1200 m, the relative humidity is uniform and equal to RH_{bel} and RH_{abv}, respectively. The initial water vapor mixing ratio profile is calculated from the temperature and relative humidity profiles, and the simulation is initialized without any liquid or ice condensate.

The formation of graupel, hail, aggregates, snow, and rain is prohibited in all simulations. Graupel and hail are prohibited because heavy riming is unlikely in these newly formed Arctic stratocumuli. Aggregation is prohibited to simplify the representation of ice microphysical processes, and the snow category is removed because it is unnecessary to represent ice crystals with shapes and densities that change with time. Finally, the formation of rain is prohibited because, although drizzle is often observed in Arctic stratocumuli (Verlinde et al. 2013), modeling studies have suggested that the effects of ice precipitation outweigh the effects of drizzle on the evolution of Arctic stratocumuli (Solomon et al. 2014). Because the objective of the study is to focus on the sensitivities of first-order processes, the inclusion of drizzle is unnecessary.

A subsidence profile is imposed such that the mean vertical velocity is -3.6 mm s^{-1} above 1000 m and decreases linearly from 0 mm s^{-1} at the surface to -3.6 mm s^{-1} at 1000 m. The west-east and south-north components of the geostrophic wind are held at 3 m s^{-1}, and the wind components are initially set equal to their geostrophic values at all altitudes. Surface sensible and latent heat fluxes are specified as 0 W m^{-2} because all simulated Arctic stratocumuli remain dynamically decoupled from the surface and do not directly interact with the surface fluxes. Only the effects of longwave radiation are included in order to simplify the analysis, and the number concentration of cloud droplets is held at a constant value of 10^8 m^{-3} in all cloudy grid cells. The simulations are run for a total of ten hours. The domain extends from 0 m to 2000 m with the vertical grid point separation set to 10 m. The model time steps for the dynamical, microphysical,

and thermodynamic calculations are five seconds, while the radiative fluxes are recalculated every ten seconds.

In total, three sets of simulations are run to test the sensitivities of the formation process to the availability of moisture, the background static stability, and the ice precipitation rate. *Set1* is used to test the formation processes' sensitivities to moisture availability and precipitation rate. *Set2* tests the sensitivities of the entrainment rates to the background static stability. Finally, *Set3* is used to determine how sensitivities to moisture availability change with background static stability. Details on the values of RH_{bel}, RH_{abv}, dT/dz, and N_{ice} used to initialize each simulation in each set are shown in Table 1; each set contains simulations with every possible combination of the parameters listed in Table 3-1.

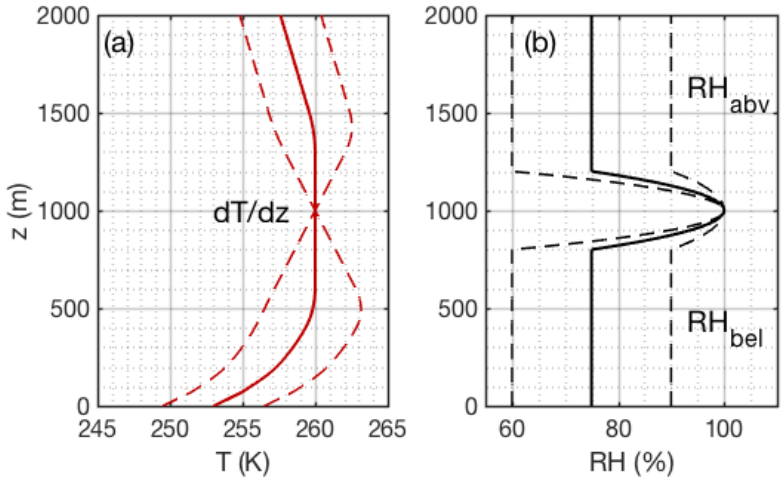

Figure **3-1**: General format for the profiles of (a) temperature and (b) relative humidity used to initialize all SCM simulations. The vertical temperature gradient between 600 m and 1300 m is labeled with 'dT/dz'. The relative humidity for $z \leq 800$ m is labeled with 'RH_{bel},' while the relative humidity for $z \geq 1200$ m is labeled with 'RH_{abv}.' Several profiles of temperature and relative humidity are plotted to show how the thermodynamic profiles change when dT/dz, RH_{bel}, and RH_{abv} are varied.

Table **3-1**: Description of the important parameters used to initialize simulations in *Set1*, *Set2*, and *Set3*. An entry in the form X:Y:Z indicates that the parameter ranges from X to Z by an interval of Y. An entry in the form A, B indicates that the parameter is either A or B, depending on the simulation.

Set name	Number of simulations	RH_{bel} (%)	RH_{abv} (%)	dT/dz (K km^{-1})	N_{ice} (L^{-1})
Set1	1156	15:5:95	15:5:95	0	0:1:3
Set2	17	75	85	-8:1:8	0
Set3	578	15:5:95	15:5:95	-7, 7	0

Drivers of cloud formation and early evolution in Arctic mixed-phase stratocumuli

McInnes and Curry (1995), Zhang (1999), and Garrett et al. (2009) outline the formation of liquid-only summertime Arctic stratocumulus. However, they do not explain the role ice plays in the formation of Arctic mixed-phase stratocumulus clouds. In this section, a baseline simulation with RH_{abv} = 85%, RH_{bel} = 75%, dT/dz = 0 K km^{-1}, and N_{ice} = 1 L^{-1} is used to describe the processes that govern the formation of Arctic stratocumulus clouds that precipitate ice. In the analysis, a mixed layer is defined as a region in which the turbulent kinetic energy exceeds 0.02 m^2 s^{-2} and the ice-liquid potential temperature varies by less than 0.2 K. These thresholds were arbitrary but allow for the effective identification of cloud-driven mixed layers. The entrainment rates at the mixed layer boundaries are calculated using the following equations:

$$w_{e,t} = \frac{d(z_t)}{dt} - \overline{w}(z_t) \qquad (5)$$

and

$$w_{e,b} = -\left[\frac{d(z_b)}{dt} - \overline{w}(z_b)\right], \qquad (6)$$

where $w_{e,t}$ is the entrainment rate at the mixed layer top, $w_{e,b}$ is the entrainment rate at the mixed layer base, z_t is the height of the mixed layer top, z_b is the height of the mixed layer base, and $\overline{w}$ is the mean subsidence velocity. The time derivatives of the mixed layer boundaries are averaged

over a sixty-minute window. The definitions of $w_{e,t}$ and $w_{e,b}$ ensure that both are positive when the mixed layer expands.

The baseline simulation shows that Arctic stratocumulus clouds that precipitate ice form by a sequence of events that is similar to the one described by McInnes and Curry (1995), Zhang (1999), and Garrett et al. (2009). Immediately after the simulation begins, radiative cooling results in the condensation of water vapor and formation of a thin cloud layer around 1000 m (Figure 3-2b,c). The condensate formation rapidly increases the layer's emissivity, and the rate at which the cloud layer cools by radiative flux divergence increases from < 2 K day^{-1} at the first time step to 40 K day^{-1} ten minutes later (Figure 3-2b,c,h). This, in turn, accelerates the condensation rate and allows the layer to rapidly gain liquid by the radiation-condensation feedback described by Zhang (1999) and Garrett et al. (2009). The increase in liquid water path (LWP) stops between simulation hours one and three, but then resumes after hour three (Figure 3-3). After six hours, the cloud thickness is 240 m and its LWP 23.5 g m^{-2} (Figures 3-2c, 3-3). Cloud top temperature and water vapor mixing ratio inversions form naturally through cooling and condensation that occur during the first half hour and strengthen during the remainder of the simulation (Figure 3-2a,b).

Thermal destabilization by radiative cooling leads to the development of turbulence in the cloud layer by the thirtieth minute of the simulation. Over the following six hours, the turbulence intensifies and an elevated mixed layer forms (Figure 3-2e,f,g). As the turbulence intensifies, the mixed layer grows very rapidly: between simulation hours one and two, the average entrainment rate at mixed layer base is 26.3 mm s^{-1}, and at mixed layer top is 9.0 mm s^{-1}. This allows the mixed layer to extend well below cloud base. However, the rate of mixed layer expansion slows considerably over the following hours: between the simulation's fifth and sixth hours, the average entrainment rates at mixed layer base and top are 7.6 mm s^{-1} and 6.6 mm s^{-1}, respectively. Within the mixed layer, turbulence mixes out most, but not all, vertical variation in liquid conserved

quantities such as the liquid potential temperature (θ_l) and vapor-plus-liquid mixing ratio ($r_{vl} = r_v + r_l$, where r_v and r_l are the water vapor and liquid mixing ratios, respectively). Therefore, profiles of these liquid conserved quantities are nearly uniform within the mixed layer, and the profile of cloud water mixing ratio is approximately moist adiabatic (Figure 3-2c,e,f).

In general, ice nucleates within the cloud, grows within the mixed layer, and then falls into and sublimates within the region below the mixed layer's base (Figure 3-2d). However, a significant amount of ice does not form until the cloud-driven mixed layer has developed. This is because turbulent motions increase in-cloud residence times of the crystals, allowing them to grow larger through depositional growth. The ice water path (IWP) increases throughout the simulation and peaks at 4 g m^{-2} near the end of the simulation (Figure 3-3).

The evolution of the stratocumulus layer's LWP can be understood through an analysis of the mixed layer's budgets of θ_l and r_{vl}. This approach has been applied to studies of stratocumulus clouds in subtropical environments (Lilly 1968; Stevens et al. 1998; Caldwell and Bretherton 2009), and can be directly applied to the cloud layer in the baseline simulation because its cloud-driven mixed layer contains nearly uniform profiles of θ_l and r_{vl} (Figure 3-2e,f). In the SCM, the mixed layer's budgets of θ_l and r_{vl} can be written as follows:

$$\frac{d\theta_{lM}}{dt} = \frac{1}{\int_{z_b}^{z_t} \overline{\rho} dz} \int_{z_b}^{z_t} \left[-\overline{\rho}\,\overline{w}\frac{\partial \overline{\theta_l}}{\partial z} - \overline{\rho}\frac{\partial}{\partial z}\left(\overline{w'\theta_l'}\right) - \frac{1}{c_p}\left(\frac{p_0}{\overline{p}}\right)^{\frac{R}{c_p}} \frac{\partial \overline{F_{net}}}{\partial z} + \overline{\rho}\frac{L_s}{c_p}\left(\frac{p_0}{\overline{p}}\right)^{\frac{R}{c_p}} \left.\frac{d\overline{r_i}}{dt}\right|_{d,s,f,m} \right] dz \quad (7)$$

and

$$\frac{dr_{vlM}}{dt} = \frac{1}{\int_{z_b}^{z_t} \overline{\rho} dz} \int_{z_b}^{z_t} \left[-\overline{\rho}\,\overline{w}\frac{\partial \overline{r_{vl}}}{\partial z} - \overline{\rho}\frac{\partial}{\partial z}\left(\overline{w'r_{vl}'}\right) - \overline{\rho}\left.\frac{d\overline{r_i}}{dt}\right|_{d,s,f,m} \right] dz, \quad (8)$$

where θ_{lM} is the mixed layer's average θ_l, r_{vlM} is the mixed layer's average r_{vl}, ρ is the density of air, p is the atmospheric pressure, F_{net} is the net radiative flux, c_p is the specific heat of dry air at constant pressure, p_0 is the reference pressure (1000 hPa) used to calculate θ_l, R is the dry air gas constant, and L_s is the enthalpy of sublimation of water. $\overline{w'\theta_l'}$ and $\overline{w'r_{vl}'}$ denote the vertical

turbulent fluxes of θ_l and r_{vl}, respectively, while $\left.\frac{d\overline{r_i}}{dt}\right|_{d,s,f,m}$ represents the tendency in the average ice mixing ratio due to deposition, sublimation, freezing, and melting. When multiplied by the coefficient outside the integral, the four added terms on the right-hand side of Eq. 7 represent, from left to right, the tendencies in θ_{lM} due to subsidence, turbulent flux convergence, radiative flux convergence, and the formation/destruction of ice. The three terms corresponding terms on the right-hand side of Eq. 8 represent the tendencies in r_{vlM} due to subsidence, the turbulent flux convergence, and the formation/destruction of ice. Independent increases in θ_{lM} and decreases in r_{vlM} result in the erosion of liquid within the cloud layer, while independent decreases in θ_{lM} and increases in r_{vlM} result in the opposite.

Figure 3-4a shows time series of each term of the r_{vl} budget (Eq. 8) during the duration of the baseline simulation. The budget terms are only plotted after the simulation's fortieth minute because the simulation does not develop a region of uniform ice-liquid potential temperature (required for the classification of the mixed layer) until that time. The budget shows that the turbulent flux convergence term has a very strong drying effect during the first three hours of the simulation, as entrainment at mixed layer base rapidly draws dry air into the mixed layer. Over the following hours, drying by entrainment occurs more slowly because entrainment at the mixed layer base slows. By the simulation's fifth hour, entrainment at the mixed layer base is too weak to counteract moistening through entrainment at the mixed layer top, and the total effect of the turbulent flux convergence term is to slightly moisten the mixed layer. In addition, the budget shows that the formation of ice (through deposition) dries the mixed layer consistently once the mixed layer forms, as deposition onto ice crystals removes vapor from the mixed layer. Meanwhile, the destruction (sublimation) of ice has a much weaker moistening effect, which only emerges after the simulation's third hour when the lower portion of the mixed layer becomes

subsaturated with respect to ice. Finally, the budget indicates that subsidence has only a weak moistening effect on the mixed layer.

Figure 3-4b shows the time series of each term of the mixed layer's θ_l budget (Eq. 7). The budget is dominated by the mixed layer's radiative cooling. The effect of radiative cooling on the mixed layer's average θ_l is most intense near the beginning of the simulation when cooling is concentrated over a shallow mixed layer with low heat capacity. This effect weakens as the mixed layer thickens, despite increases in the layer's emissivity and maximum local radiative cooling rate (Figure 3-2h). The turbulent flux convergence has a weak but consistent warming effect on the mixed layer because the downward flux of θ_l at the mixed layer top exceeds the downward flux of θ_l at the mixed layer base. The ice formation term also has a weak warming effect as latent heat is released during deposition. Both subsidence and latent cooling during sublimation play minor roles in the mixed layer's θ_l budget.

The budgets of θ_l and r_{vl} after hour six in the baseline simulation are qualitatively similar to the water mass and sensible heat budgets of a precipitating Arctic stratocumulus layer presented by Sulia et al. (2014). In both cases, radiative cooling dominates the layer's budget of sensible heat, ice precipitation dominates the layer's budget of water mass, and turbulent/advective processes play small roles in the budgets of both sensible heat and water mass. However, the turbulent/advective terms in the water mass budgets have opposite signs in the two simulations. This is most likely because a r_t inversion is present above mixed layer top in the baseline simulation, but not in the simulation by Sulia et al. (2014). This allows entrainment to serve as a source of moisture in the baseline simulation, and as a sink of moisture in the simulation by Sulia et al. (2014).

Figure 3-5 illustrates the effects of ice precipitation on the cloud-driven mixed layer in greater detail. These effects may be broken down into one primary and three secondary effects, which are labeled with numbers 1-4 in Figure 3-5. The primary effect is to dry and warm the

mixed layer through the removal of vapor and the release of latent heat. The first secondary effect compensates partially for the warming/drying effect. After simulation hour three, ice sublimates in the lower portion of the cloud-driven mixed layer (Figure 3-5), restoring vapor to and removing heat from mixed layer. Both the primary and first secondary effects on the cloud layer's evolution are clearly visible in Figure 3-4, and are well documented in modeling studies by Morrison et al. (2011b), Solomon et al. (2014), and Sulia et al. (2014).

The second secondary effect is not so clearly visible in Figure 3-4. After passing through the mixed layer's base, ice precipitation sublimates in the region directly below (Figure 3-5). This moistens and cools this lower region and influences the cloud layer's evolution by modifying the properties of air that the mixed layer eventually entrains (similar to drizzle in warm stratocumulus, Stevens et al., 1998). A comparison of this simulation with an identical simulation without ice indicates that this modification has an appreciable effect on the mixed layer's budgets of θ_l and r_{vl}. At simulation time 3 hrs and altitude 625 m (which lies 50 m below mixed layer base in the ice-free simulation), r_{vl} is 0.04 g kg^{-1} higher and θ_l is 0.14 K lower in the baseline simulation than in the simulation without ice. By simulation hour six, these differences 50m below mixed layer base in the ice-free simulation grow to 0.08 g kg^{-1} and 0.27 K, respectively. Back-of-the-envelope calculations indicate that the cooling and moistening through the sublimation of ice precipitation below the mixed layer base offsets 15-25% of the drying/warming that occurs during ice formation. The effect is even more substantial when the atmosphere is drier below the mixed layer base and when ice precipitation is heavier, because more precipitation sublimates below mixed layer base under such conditions.

The final secondary effect is also not so clearly visible in Figure 3-4. A comparison of the simulations with and without ice indicates that ice precipitation slows entrainment at both the mixed layer base and top. After six hours, the mixed layer base and top in the baseline simulation lie at 560 m and 1100 m, respectively, while the mixed layer base and top in the ice-free

simulation lie at 520 m and 1110 m, respectively. Because entrainment has a strong drying effect on the mixed layer in the baseline simulation, the decrease in entrainment rates slows the rate at which the mixed layer dries. Entrainment at mixed layer base slows because the sublimation of ice near mixed layer base stabilizes that region, making it more difficult for turbulence to entrain air from below the mixed layer base. The cause for the slight decrease in the entrainment rate at the mixed layer top is less clear. However, both the removal of liquid through the growth of ice precipitation near mixed layer top and the baseline simulation's lower LWP may contribute. A similar effect of ice precipitation on the mixed layer's entrainment rates is present in large eddy simulations by Solomon et al. (2014).

The budget analysis presented above indicates that newly formed Arctic stratocumuli evolve in three basic stages. A schematic of these three stages is presented in Figure 3-6. In the first stage, liquid within the cloud layer forms rapidly through the radiation-condensation feedback described by Zhang (1999) and Garrett et al. (2009). During this period, ice has a small influence on the cloud layer's evolution because depositional growth of ice crystals is slow. The second stage begins when the cloud-driven mixed layer forms and begins to rapidly expand. During this stage, entrainment is very rapid, particularly at the mixed layer base and significant ice begins to form. Both entrainment and ice precipitation may severely modify the mixed layer's thermodynamic properties and the cloud layer's LWP. In the baseline simulation, entrainment and ice precipitation almost perfectly balance the effect of radiative cooling and the layer's LWP remains approximately constant. As entrainment at the mixed layer base slows, the cloud gradually transitions to the third stage of its formation. In this third stage, the effects of radiation, entrainment, and ice precipitation are nearly constant with time. Radiative cooling continues to drive cloud growth by cooling the cloud layer and forcing vapor to condense, while ice precipitation counters cloud growth by warming and drying the mixed layer. Entrainment has a smaller overall effect because entrainment occurs more slowly. This balance between the effects

of radiation, precipitation, and entrainment is very similar to the balance Morrison et al. (2011b), Sulia et al. (2014), and Solomon et al. (2014) describe as governing the evolution of more mature Arctic mixed-phase stratocumulus clouds.

Because the competing effects of radiation, entrainment, and ice precipitation control the formation of Arctic stratocumuli, the formation of Arctic stratocumuli must be sensitive to changes in the moisture availability, the background static stability, and the ice precipitation rate. In the next sections of this chapter, the simulations in *Set1*, *Set2*, and *Set3* are used to examine each of these sensitivities.

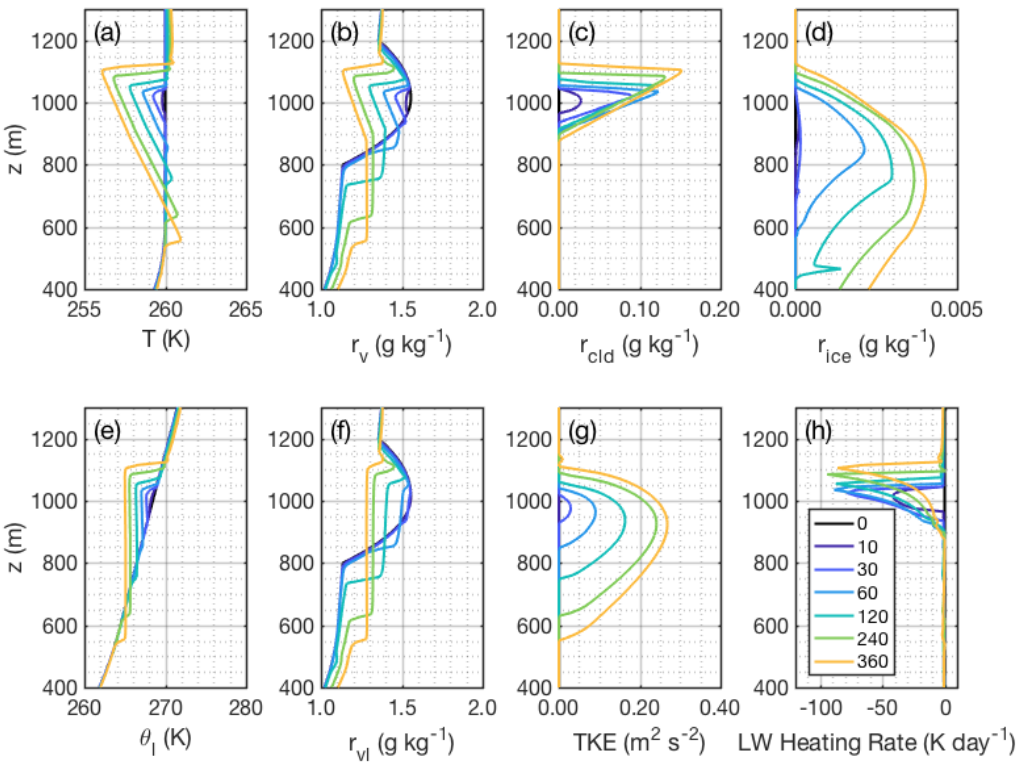

Figure **3-2**: Profiles of (a) temperature, (b) water vapor mixing ratio, (c) cloud water mixing ratio, (d) ice mixing ratio, (e) liquid potential temperature, (f) vapor-plus-liquid mixing ratio, (g) turbulent kinetic energy, and (h) local longwave heating rate at various times during baseline simulation. The profiles are plotted 0, 10, 30, 60, 120, 240, and 360 minutes after the beginning of the simulation; the colors corresponding to each time are shown in the legend in (h).

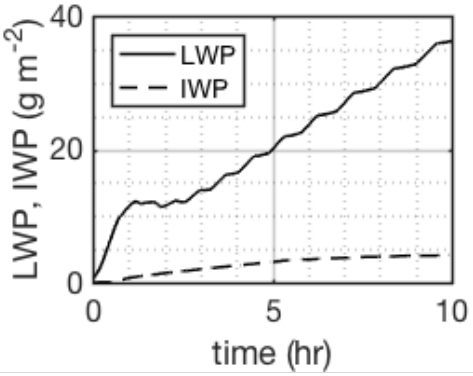

Figure **3-3**: Time series of liquid water path (LWP) for the baseline simulation.

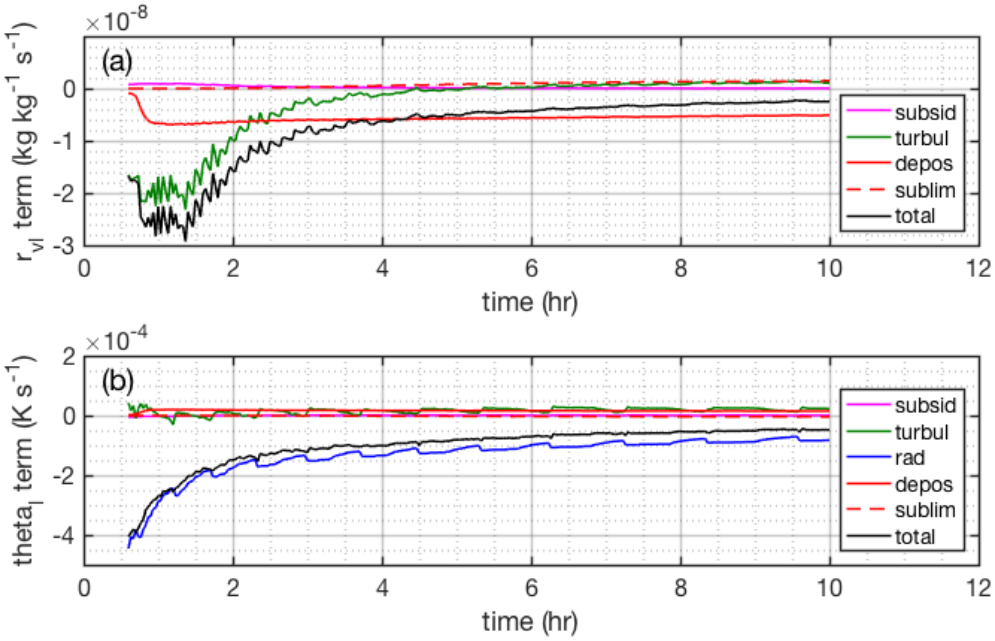

Figure **3-4**: Time series of each budget term for (a) r_{vl} and (b) θ_l over the entire ten hours of the baseline simulation. The magenta lines show time series of the subsidence term, the green lines of the turbulent term, the blue line of the radiation term, and the red lines of the ice formation/destruction term. The ice formation/destruction term is split in two: the solid line shows the effect of ice formation through deposition, while the dashed shows the effect of ice destruction through sublimation. Neither freezing of liquid nor melting of ice occurs in the simulation.

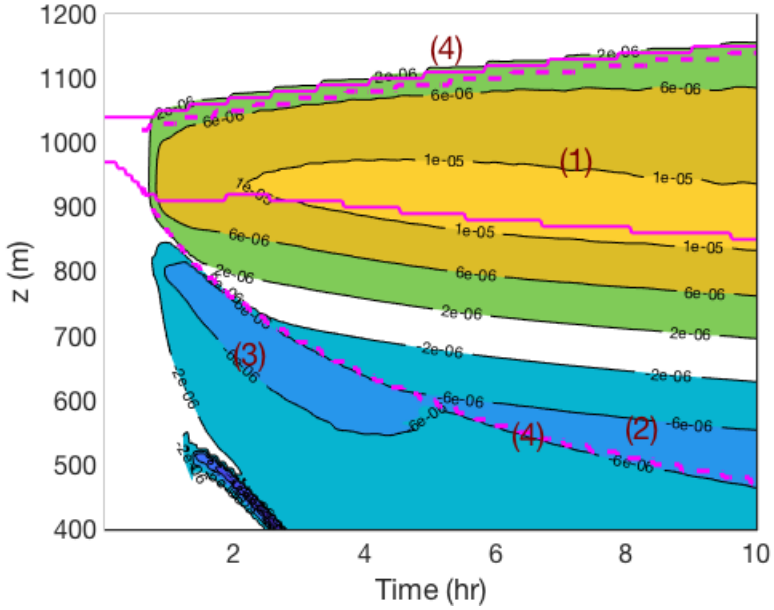

Figure **3-5**: Illustration of the primary and three secondary effects of ice precipitation on the formation process in the baseline simulation. Time series of the cloud boundaries are plotted in solid magenta, while time series of the mixed layer boundaries are plotted in dashed magenta. Time series of the profiles of the depositional growth rate of ice precipitation (g kg^{-1} s^{-1}) are contoured. Yellow and green colors indicate depositional growth, while blue colors indicate sublimation. The primary drying effect of ice precipitation is labeled with "(1)". The first, second, and third secondary effects are labeled with "(2)", "(3)", and "(4)", in the order that they are presented in the text.

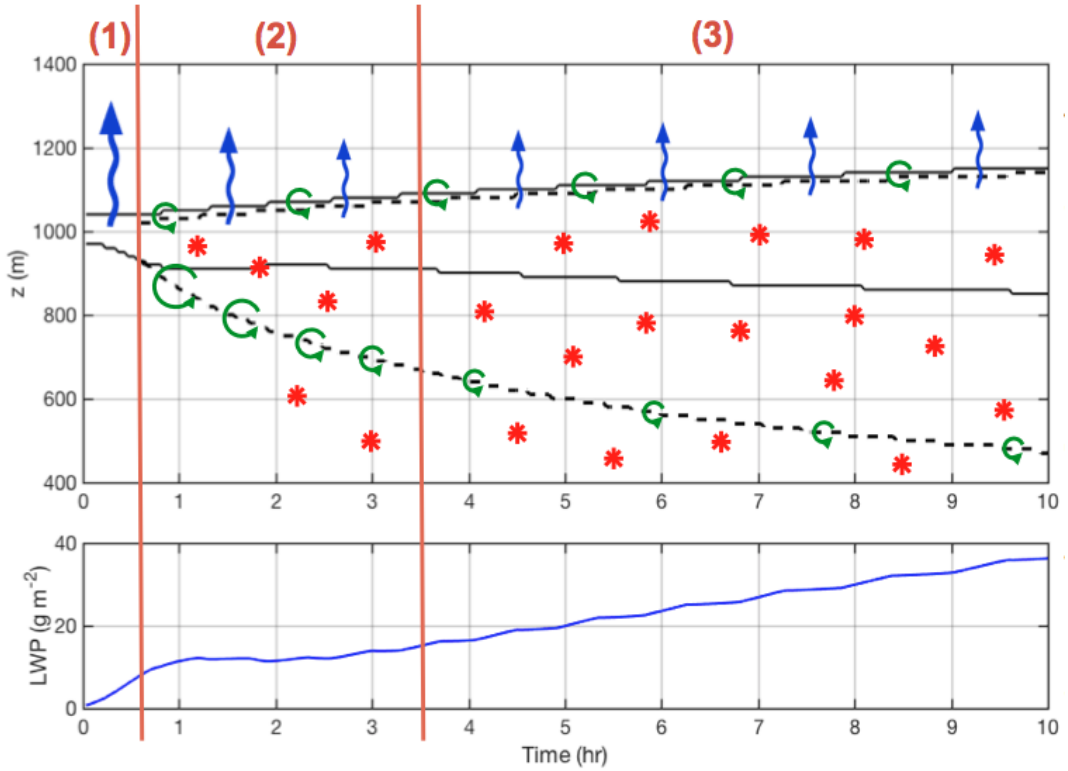

Figure **3-6**: Schematic of the three basic stages of the formation of elevated, mixed-phase Arctic stratocumuli in advecting air masses. The top panel shows time series of the cloud boundaries (solid) and mixed layer boundaries (dashed), while the bottom panel shows the time series of LWP for the baseline simulation. The three stages are separated using vertical lines and are labeled with the numbers 1-3. Blue arrows represent radiative cooling of the cloud-driven mixed layer, red stars represent ice precipitation, and green circular arrows represent entrainment. Larger blue arrows indicate more rapid cooling of the mixed layer through radiative cooling, while larger green circular arrows indicate more rapid entrainment at the mixed layer boundary.

Sensitivity to moisture availability above and below

The effect of moisture availability on Arctic stratocumulus formation is demonstrated most clearly through an examination of all simulations in *Set1* for which $N_{ice} = 0\ L^{-1}$. Simulated clouds in this set may be loosely subdivided into three groups, which achieve radiatively distinct outcomes. The first group consists of cloud layers that deepen through a majority of the simulation and attain LWPs over 20 g m^{-2} by the end of the simulation, operating nearly as

blackbodies (Shupe and Intrieri 2004). The second group consists of clouds that grow through most of the simulation but do not grow as deep, attain LWPs between 2 g m^{-2} and 20 g m^{-2}, and operate as graybodies at the end of the simulation. The final group consists of clouds that lose a majority of their liquid to the entrainment of dry air during the second stage of the formation process, and either dissipate or enter a quasi-steady state with a LWP of less than 2 g m^{-2}. Combinations of RH_{abv} and RH_{bel} that produce clouds in the first, second, and third groups are shaded in white, light gray, and dark gray/black in Figure 3-7a, respectively.

Clouds in the first group typically form in environments with large RH_{bel}. They become very optically thick, operate nearly as blackbodies, and result in downwelling longwave irradiances (DLIs) of over 230 W m^{-2} (Figure 3-7b). The LWPs of these clouds are strong functions of RH_{bel} and weaker functions of RH_{abv}. Between simulation hours 2-3, the clouds' LWPs range from 6 g m^{-2} to 55 g m^{-2}, and are sensitive almost exclusively to RH_{bel} (Figure 3-8a). This is because entrainment at mixed layer base is much more rapid than entrainment at mixed layer top (Figure 3-9a,c), so that the properties of air below the mixed layer have a far greater influence on the mixed layer's composition. However, the LWPs of clouds with $RH_{abv} \geq 80\%$ are also sensitive to RH_{abv}. This is because entrainment rates at mixed layer base are several mm s^{-1} smaller, and entrainment rates at mixed layer top are several mm s^{-1} larger, than in simulations for which $RH_{abv} < 80\%$ (Figure 3-9a,c). This allows properties of the air above to have a greater influence on mixed layer composition. Between simulation hours 8-9, the average LWPs of the clouds in this first group range from 18 g m^{-2} to 155 g m^{-2}. Although LWP is still more sensitive to RH_{bel} than RH_{abv}, the difference in the sensitivities is smaller because the entrainment rates at the mixed layer base and top become more equal in magnitude as the simulation progresses (Figure 3-9b,d).

Clouds in the second group typically form in environments with slightly lower RH_{abv} and RH_{bel}. They evolve similarly to the clouds in the first group, but are not able to grow as deep

because the entrained air is drier. Consequently, they become less optically thick, operate as graybodies, and result in DLIs that range from 170 W m^{-2} to 230 W m^{-2} and increase commensurately with the layer's LWP (Figure 3-7b). The number of clouds in the second group is much smaller than the number of clouds in the first and third groups. This suggests that the buffer between the optically thick clouds in the first category and optically thin clouds in the third category is narrow, and that a majority of combinations of RH_{abv} and RH_{bel} yield one of the two radiatively extreme outcomes. This is especially true for clouds that form in environments with high RH_{abv} (Figure 3-7a).

Clouds in the third group enter a low-LWP quasi-steady state through a negative feedback between entrainment and radiative cooling. During the second stage of each cloud layer's development, the mixed layer entrains dry air from below very quickly. This decreases the cloud's LWP, emissivity, and radiative cooling rate, and therefore slows the generation of turbulence. Consequently, turbulence within the mixed layer weakens and the entrainment of dry air slows. As the cloud layer's LWP falls below 2 g m^{-2}, the effects of entrainment and radiative cooling come into balance and the cloud layer enters a quasi-steady state. In this quasi-steady state, entrainment is unable to remove liquid because turbulence is only generated when liquid is present. Radiative cooling is also unable to produce additional liquid because the additional liquid drives an acceleration of entrainment, which dries the mixed layer and destroys liquid. As a consequence, the layer's LWP remains near its equilibrium value, the cloud remains optically thin, and resulting DLIs at the surface remain below 170 W m^{-2} (Figure 3-7b).

Once a cloud layer enters the low-LWP quasi-steady state, it may remain in the quasi-steady state through the end of the simulation (shaded dark gray in Figure 3-7a) or dissipate after several hours (shaded black in Figure 3-7a). In each simulation, whether or not the cloud layer dissipates is determined by the cloud layer's response to a perturbation in the rate the mixed layer entrains dry air. After the cloud layer exists in a quasi-steady state for several hours, the cloud-

driven mixed layer expands, incorporating a new grid cell above. This expansion allows the mixed layer to temporarily entrain air from above more quickly. If the entrained air is relatively moist, only some of the remaining liquid evaporates and the cloud layer returns to the quasi-steady state. However, if the entrained air is very dry, the remaining liquid evaporates and the cloud layer dissipates. Therefore, it is very possible that this bifurcation into layers that do and do not dissipate is an artifact of the SCM's discretization of the vertical grid.

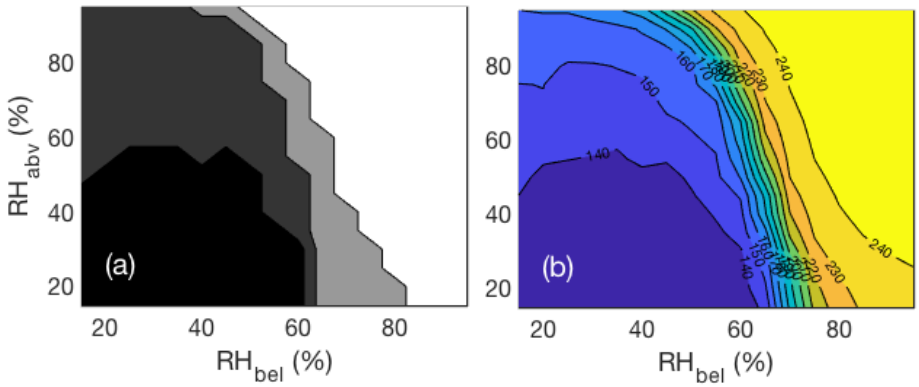

Figure **3-7**: (a) Combinations of RH_{abv} and RH_{bel} that yield clouds in each radiatively distinct group, for simulations in *Set1* with $N_{ice} = 0\ L^{-1}$. Clouds in the first group (become optically thick) are shaded in white, clouds in the second group (achieve intermediate optical thicknesses) are shaded in light gray, and clouds in the third group are shaded in either dark gray (become optically thin) or black (dissipate). (b) Contour plot of the downwelling longwave irradiance incident on the surface, averaged between simulation hours 8-9, for each combination of RH_{abv} and RH_{bel}.

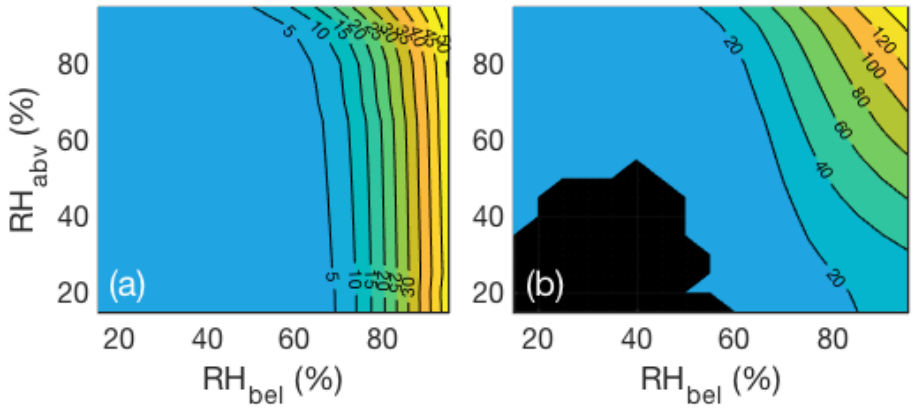

Figure **3-8**: Contour plots of LWP (g m^{-2}) as a function of RH_{abv} and RH_{bel} for simulations in *Set1* with N_{ice} = 0 L^{-1}, averaged between (a) hours 2 and 3 and (b) hours 8 and 9. Points corresponding to LWPs of 0 g m^{-2} are shaded in black.

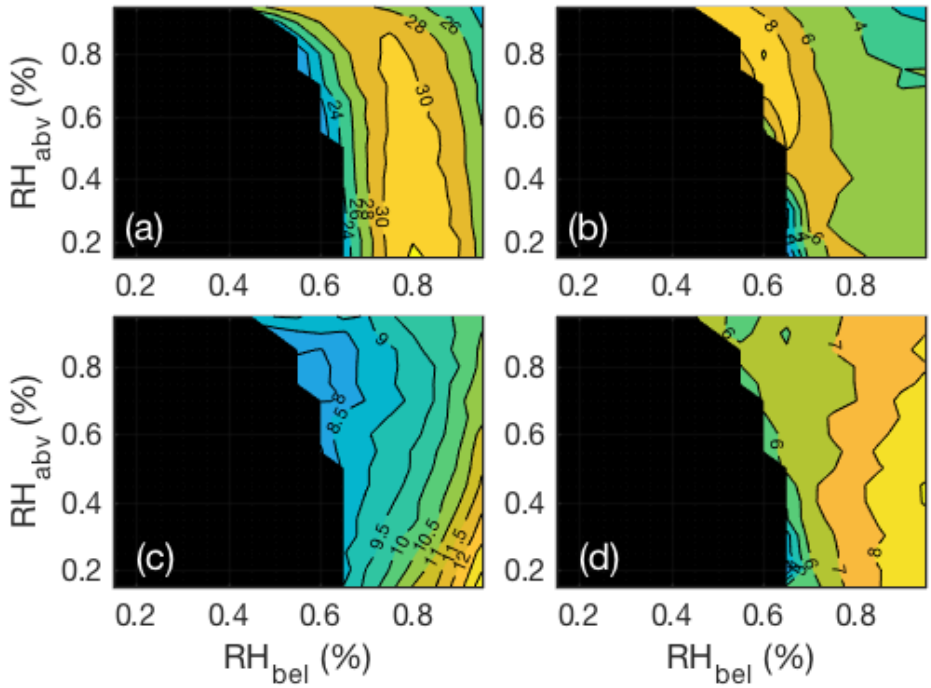

Figure **3-9**: Contour plots of the entrainment rates (mm s^{-1}) at mixed layer base (first row) and mixed layer top (second row) as a function of RH_{abv} and RH_{bel} for simulations in *Set1* with N_{ice} = 0 L^{-1}, averaged between simulation hours 1 and 2 (first column) and hours 7 and 8 (second column). Entrainment rates are positive when the mixed layer expands. Points corresponding to simulations with clouds that either enter the low-LWP quasi-steady state or dissipate are shaded in black.

Sensitivity to static stability

Static stability affects the formation of Arctic stratocumuli through its effect on the entrainment rates. Figure 3-10 shows the entrainment rates at mixed layer base and top as a function of the vertical temperature gradient at 1000 m (dT/dz) for all simulations in *Set2*. Separate plots are included for the average entrainment rates between simulation hours 1-2 (period of most rapid entrainment) and hours 6-9 (after entrainment has slowed). According to the SCM simulations in *Set2*, the entrainment rates at mixed layer base and top between hours 1-2 and at mixed layer top between hours 6-9 all decrease with increasing static stability. This is expected: when Arctic stratocumuli form in regions that are less statically stable, less work against buoyant forces is required for turbulence to entrain air from above and below the mixed layer, and entrainment occurs more quickly. Conversely, when Arctic stratocumuli form in regions that are more statically stable, more work against buoyant forces is required and entrainment occurs more slowly.

However, the average entrainment rate at the mixed layer base between hours 6-9 behaves unexpectedly: it peaks when dT/dz = 0 K km^{-1} and decreases under conditions of both lower and higher static stability. A more detailed examination of the simulations in *Set2* indicates that the decrease in the entrainment rate with decreasing static stability occurs because the mixed layer penetrates into the surface-based temperature inversion. The mixed layers in simulations with lower static stability extend deeper into the surface inversion because they expand more rapidly during the first portion of the simulation. Static stability increases towards the surface in the surface inversion (Figure 3-1a), and so entrainment at mixed layer base is suppressed more strongly in simulations with lower dT/dz between 600 m and 1300 m.

Through its effect on the entrainment rates, static stability has a strong effect on the formation process' sensitivities to the availability of moisture above and below. These

sensitivities are best demonstrated through a comparison of the simulations in *Set3* (dT/dz = $\pm$7 K km^{-1}, N_{ice} = 0 L^{-1}) with simulations in *Set1* (dT/dz = 0 K km^{-1}, N_{ice} = 0 L^{-1}). When dT/dz = -7 K km^{-1}, entrainment is more rapid at the mixed layer base and top. In addition, radiative cooling of the mixed layer slows because cooling is spread over a greater depth with larger heat capacity (Figure 3-11a). Consequently, the cloud layers become more sensitive to RH_{abv} and RH_{bel}. Fewer clouds become optically thick (LWP > 20 g m^{-2}) because the cloud layers are less resilient to the presence of dry air above and below (Figure 3-12a). However, the clouds in the moistest environments attain higher LWPs than when dT/dz = 0 K km^{-1} because moist air is entrained much more rapidly (Figure 3-12c). The LWPs of the optically thick clouds are also more evenly sensitive to RH_{abv} and RH_{bel} because the entrainment rates at the mixed layer base and top are more even in magnitude (Figure 3-7). Very few clouds end the simulation with LWPs between 2 g m^{-2} and 20 g m^{-2} (Figure 3-12a). This indicates that individual combinations of RH_{abv} and RH_{bel} under conditions of low static stability are much more likely to yield one of the radiatively extreme outcomes, and less likely to yield the moderate outcome. Finally, many more combinations of RH_{abv} and RH_{bel} yield clouds that either remain optically thin or dissipate. Unlike when dT/dz = 0 K km^{-1}, all of these clouds dissipate before the end of the simulation (Figure 3-12a).

When dT/dz = +7 K km^{-1}, entrainment occurs more slowly at the mixed layer base and top. The mixed layer also cools more quickly because radiative cooling is spread over a smaller depth (Figure 3-11b). Consequently, the cloud layers are less sensitive to RH_{abv} and RH_{bel}. A higher number of combinations of RH_{abv} and RH_{bel} yield clouds that become optically thick (Figure 3-12b). The optically thick clouds generally attain higher LWPs than when dT/dz = 0 K km^{-1} because radiative cooling of the mixed layer occurs more rapidly (Figure 3-12d). A higher number of clouds also end in the intermediate outcome (Figure 3-12b), indicating that individual combinations of RH_{abv} and RH_{bel} are less likely to yield one of the radiatively extreme outcomes.

Finally, fewer combinations of RH_{abv} and RH_{bel} yield clouds that are very optically thin, and none of these clouds dissipate before the end of the simulation (Figure 3-12b).

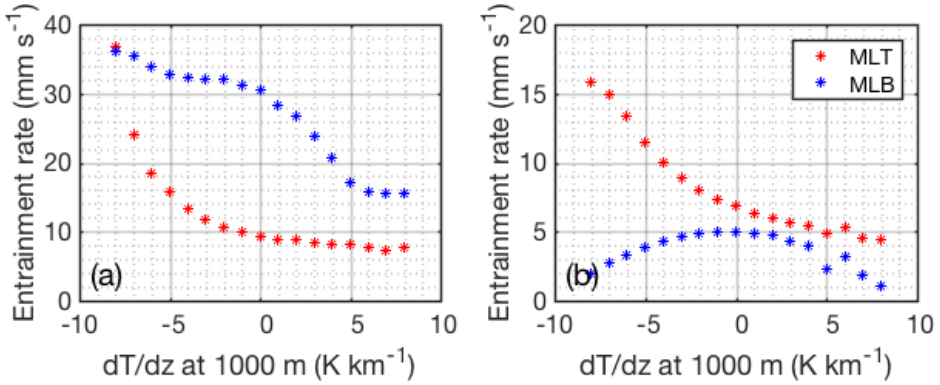

Figure **3-10**: Entrainment rate at mixed layer base (MLB) and top (MLT) averaged between simulation hours (a) 1 and 2, and (b) 6 and 9, as a function of the vertical temperature gradient at the initial point of saturation.

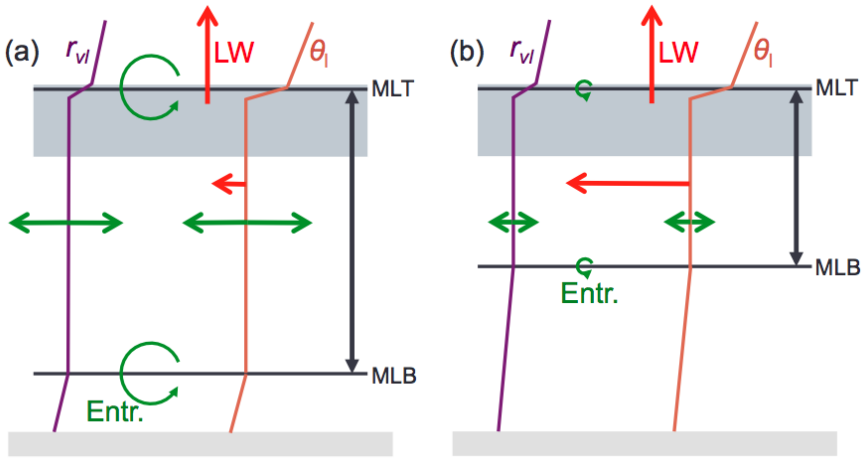

Figure **3-11**: Schematic diagrams of how a (a) decrease and (b) increase in static stability affect the mixed layer budgets of θ_l and r_{vl}, and therefore the formation of Arctic stratocumuli. Decreases in static stability accelerate entrainment at both mixed layer base and top, decrease the rate the mixed layer cools through radiative cooling, and therefore decrease a cloud layer's resilience to dry air above and below. Increases in static stability slow entrainment, increase the rate at which the mixed cools through radiative cooling, and therefore increase a cloud layer's resilience to dry air above and below.

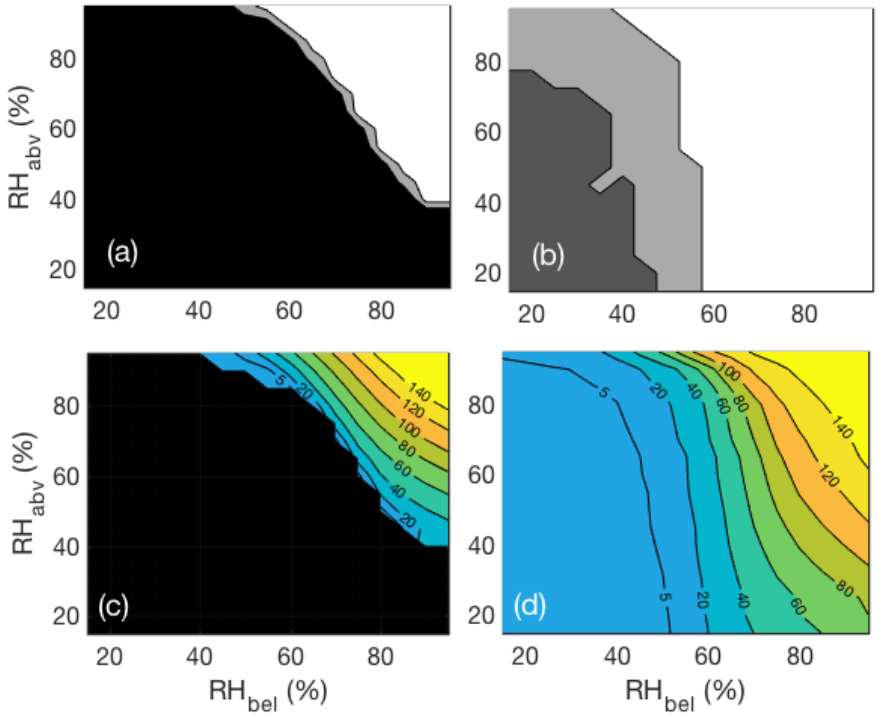

Figure **3-12**: Top row: equivalent to Figure 3-7a, but for simulations in *Set3* with (a) dT/dz = -7 K km^{-1} and (b) dT/dz = +7 K km^{-1}. Bottom row: contour plots of LWP (g m^{-2}) as a function of RH$_{abv}$ and RH$_{bel}$ for simulations in *Set3* with (c) dT/dz = -7 K km^{-1} and (d) dT/dz = +7 K km^{-1}, averaged between hours 8 and 9. Points corresponding to LWPs of 0 g m^{-2} in (c) and (d) are shaded in black.

Sensitivity to ice precipitation rate

The introduction of a small number of ice crystals (N_{ice} = 1 L^{-1}) allows the cloud layers to precipitate ice lightly, and affects the LWPs of cloud layers that acted as black- and graybodies in simulations with N_{ice} = 0 L^{-1} (Figure 3-7a and 3-8b). These clouds generally attain lower LWPs because the ice precipitation suppresses the growth of liquid (Figure 3-13c). Therefore, many cloud layers that operated as blackbodies when N_{ice} = 0 L^{-1} operate as graybodies when light ice precipitation is introduced (Figure 3-13a). In addition, their LWPs are less sensitive to the initial

RH_{bel} because the deposition/sublimation of ice precipitation below the mixed layer base pushes the relative humidity with respect to ice towards 100% as each simulation progresses (Figure 3-13c).

The effect of light ice precipitation on clouds that remain optically thin or dissipate is subtler. Several additional combinations of RH_{abv} and RH_{bel} yield clouds that enter the low-LWP quasi-steady state, and several additional combinations yield clouds that dissipate before the end of the simulation (Figure 3-13a). However, the breakdown of cloud layers that remain in a quasi-steady state and dissipate is similar to when $N_{ice} = 0\ L^{-1}$ (compare Figure 3-7a and Figure 3-13a). This similarity is due to a buffering feedback between the effects of ice precipitation and entrainment. When cloud layers simulated with $N_{ice} = 1\ L^{-1}$ enter a low-LWP quasi-steady state, the state is maintained by a balance between the effects of radiation, entrainment, and ice precipitation, instead of only the effects of radiation and entrainment. Comparisons of simulations that differ only in the value of N_{ice} indicate that the combined effect of entrainment and precipitation in simulations with $N_{ice} = 1\ L^{-1}$ is nearly identical to the individual effect of entrainment in the respective simulations with $N_{ice} = 0\ L^{-1}$. In other words, the introduction of light ice precipitation modifies the overall effect of entrainment such that the introduction of ice precipitation has little effect on the cloud layer's evolution.

When a larger number of ice crystals is introduced ($N_{ice} = 2\ L^{-1}$), the cloud layers precipitate ice more heavily and attain still lower LWPs because the drying effect of ice precipitation is more intense (Figure 3-13d). Thus, many layers that operated as blackbodies when $N_{ice} = 1\ L^{-1}$ operate as graybodies when $N_{ice} = 2\ L^{-1}$ (Figure 3-13b). Very few cloud layers remain in the low-LWP quasi-steady state through the end of the simulation. Instead, a vast majority of the layers dissipate (Figure 3-13b), suggesting that entrainment has only a limited ability to buffer the effects of ice precipitation on cloud layers with low LWPs. Entrainment was

able to buffer the effects of light ice precipitation, but not of the heavier ice precipitation. Each of these effects is more pronounced when N_{ice} is increased to 3 L^{-1} (not shown).

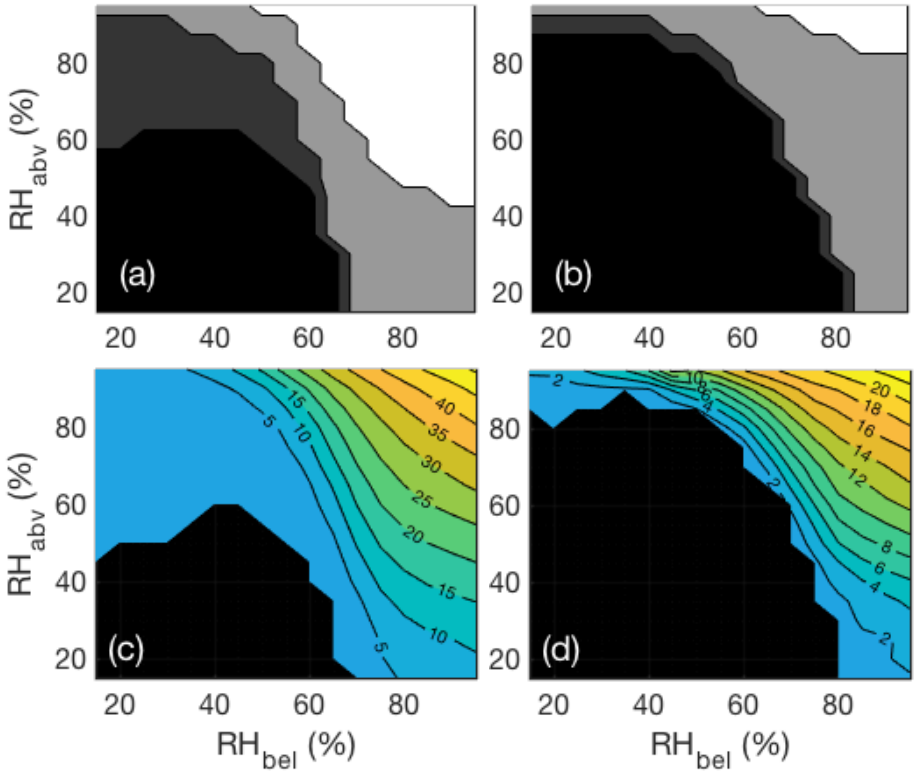

Figure **3-13**: Equivalent to Figure 3-12, but for simulations in *Set1* with (a,c) N_{ice} = 1 L^{-1} and (b,d) N_{ice} = 2 L^{-1}. Note that dT/dz = 0 K km^{-1} for the simulations.

Chapter 4

Discussion

Previous work by Herman and Goody (1976), McInnes and Curry (1995), Zhang (1999), and Garrett et al. (2009) suggests that summertime Arctic stratocumuli may form through the cooling of air masses that advect across the Arctic. Remote sensing observations from the ARM facility on the North Slope of Alaska indicate that Arctic stratocumuli must also form by this mechanism during other seasons, as well as when temperatures are low enough to support the production of ice precipitation. Radiative transfer calculations suggest that this is indeed possible, and may occur through the effects of radiative cooling, synoptic-scale lifting, or a combination of both.

Simulations with a SCM show that Arctic stratocumuli evolve in three stages after cooling forces condensation at a single elevation. In the first stage, the Arctic stratocumulus layer grows rapidly through a feedback between radiative cooling and condensation. A short time later, radiative cooling of the cloud layer drives the formation and rapid expansion of a cloud-driven mixed layer. Entrainment during this second stage is intense and may severely modify both mixed layer properties and the cloud layer's LWP. If the cloud layer survives this period of rapid entrainment, it gradually transitions to the third stage, in which it continues its growth. The effects of ice precipitation are weak during the first stage, and are more substantial during the second and third stages. Discounting the effects of ice, the formation process visible in the SCM simulations is very similar to the formation process that McInnes and Curry (1995), Zhang (1999), and Garrett et al. (2009) collectively outline.

Ice precipitation affects the cloud layer's formation through one primary and three secondary effects. The primary effect is to suppress the growth of liquid by warming and drying

the cloud-driven mixed layer. The secondary effects arise from the sublimation of ice in the lower portion of the cloud-driven mixed layer, the sublimation/growth of ice in air that is eventually entrained from below the mixed layer base, and feedbacks with the mixed layer's entrainment rates. These may either supplement or counteract the primary drying effect, depending on the availability of moisture above and below. However, the primary effect outweighs the sum of the secondary effects in all SCM simulations that allow ice precipitation. The primary effect and first secondary effect have been well documented by Solomon et al. (2014), Morrison et al. (2011b), and Sulia et al. (2014), while the third secondary effect is visible in simulations by Solomon et al. (2014), but is not explicitly discussed.

The SCM simulations also show that the formation of Arctic stratocumuli in advecting air masses may result in three radiatively distinct outcomes: one that is optically thick, one that is optically thin/radiatively clear, and one that is intermediate. When Arctic stratocumulus layers form in regions with high relative humidity above and below, high background static stability, and low concentrations of ice forming nuclei, the formation process is most likely to achieve the first outcome: an optically thick cloud layer. When the layers form in regions with low relative humidity above and below, low background static stability, and high concentrations of ice forming nuclei, they are most likely to achieve the third: a tenuous layer that either dissipates partway through the simulation or persists. Finally, when the layers form in regions with conditions in between the two extremes, they may achieve an intermediate outcome, in which the cloud layers achieve intermediate LWPs and operate as graybodies. This intermediate outcome becomes less likely as the static stability decreases, and is typically less likely than the two radiatively extreme outcomes. This finding is significant for several reasons. First, it provides a possible explanation for the bimodality in the distribution of NetLW irradiance across the Arctic in winter (Figure 1-1): when Arctic stratocumuli form in advecting air masses, wider ranges of conditions lead to the radiatively extreme outcomes than the intermediate outcome. In addition,

the finding emphasizes the need for parameterizations of Arctic stratocumuli in general circulation models that explicitly represent the effects of radiative cooling, entrainment, and ice precipitation. These three processes govern the formation, persistence, and dissipation of elevated Arctic stratocumulus cloud layers, and therefore must be captured to accurately simulate their evolution.

Results from this study should also be considered in studies of the formation of altocumulus in mid-latitudes. Liquid-only and mixed-phase altocumulus clouds are very similar to dynamically decoupled Arctic stratocumuli: both consist of a liquid layer that precipitates ice into the region below and supports an elevated mixed layer (Liu 1998; Smith et al. 2009). In addition, many altocumulus clouds form through adiabatic cooling during large-scale lifting and therefore the process outlined by these SCM simulations (Liu 1998).

More broadly, these SCM simulations provide insight into the dissipation of Arctic stratocumuli. Previous studies have shown that Arctic stratocumuli dissipate through the warming and/or drying of the cloud-driven mixed layer, which may occur through the entrainment of dry air, the enhancement of ice precipitation, the reduction in the mixed layer's radiative cooling rate, or a combination of the three (Morrison et al. 2011b, Solomon et al. 2014; Loewe et al. 2017). Large eddy simulations by Solomon et al. (2014) and Loewe et al. (2017) indicate the entrainment of dry air cannot easily drive the dissipation of mature Arctic stratocumuli. The SCM simulations suggest that this difficulty may arise from a negative feedback between radiative cooling and entrainment. As entrainment erodes liquid, turbulent motions within the cloud layer weaken, slowing the entrainment of dry air and the rate at which liquid is eroded. This permits the cloud layers to remain at low LWPs for extended periods of time instead of simply dissipating.

Furthermore, the SCM simulations suggest an alternative mechanism for the formation of cloud-top r_v inversions, which has not been thoroughly explored in the literature. Cloud-top r_v inversions are a subject of active study because they are found frequently near the tops of Arctic

stratocumuli (Sedlar and Tjernström 2009; Sedlar et al. 2012), and because they may influence the evolution of Arctic stratocumulus, the outgoing longwave irradiance at the top of the atmosphere, and a cloud layer's surface radiative forcing (Solomon et al. 2011; Sedlar et al. 2012; Solomon et al. 2014). Thus far, two mechanisms for the formation of cloud-top humidity inversions have been proposed. First, cloud-top r_v inversions may form through the detrainment of liquid water and water vapor at cloud top (Devasthale et al. 2011; Solomon et al. 2014). Second, cloud-top r_v inversions may form through differential advection of moisture near cloud top (Sedlar et al. 2012). However, the SCM simulations in this thesis suggest a third mechanism: that cloud-top r_v inversions may form as a natural consequence of the formation of Arctic stratocumuli in moist environments. As the cloud layer forms, both temperature and r_v within the cloud layer decrease through radiative cooling and the resulting condensation. Because cooling and condensation do not occur in the region above cloud top, this naturally produces a region in which r_v increases with height (an inversion). This is similar to the formation mechanism for the r_v inversion in simulations by Curry (1983).

Because parameterizations in this SCM are simplified, the formation process should be examined further with more detailed models. For example, it is likely that the discretization of the vertical grid affected the SCM's simulations of cloud layers with low LWP. The behavior of clouds with low LWPs is important because optically thin clouds do produce larger downwelling longwave irradiances than clear skies (Figure 3-7b). In addition, the SCM's specification of cloud droplet number concentration is unrealistic. If the concentration of cloud droplets were predicted from peak supersaturations in updrafts and a distribution of cloud condensation nuclei, the number concentration would likely be smallest before turbulent motions developed, and grow as the turbulent motions intensified. Therefore, the simplified parameterization could have affected rates of condensation and entrainment shortly after the cloud layer formed, potentially affecting the rates at which the first and second stages of the formation process progressed. Furthermore,

the parameterization of ice nucleation is very unrealistic, especially because it does not account for the depletion of ice nuclei or for ice nucleation by different mechanisms. Simulations by Morrison et al. (2005) and Frindlind et al. (2012) show that the inclusion of these complexities allows precipitation rates from Arctic stratocumuli to vary with time. Therefore, inclusion of these complexities in the SCM simulations could allow precipitation rates to vary during the formation process and thus alter the simulated cloud layers' early evolution.

Chapter 5

Conclusions

Remote sensing observations and radiative transfer calculations indicate that Arctic stratocumuli form through the cooling of advecting air masses during all seasons. Single column model simulations of the formation process indicate that the formation process of Arctic stratocumuli that precipitate ice is qualitatively similar to the process by which liquid-only Arctic stratocumuli form in summer (McInnes and Curry 1995; Zhang 1999; Garrett et al. 2009). However, ice does suppress the growth of liquid, through a primary drying effect and three secondary effects that arise from sublimation in the lower portion of the cloud-driven mixed layer, sublimation/depositional growth in air below the cloud-driven mixed layer that is eventually entrained, and feedbacks with entrainment rates.

In addition, the single column model simulations show that the radiative effects of Arctic stratocumuli that form in advecting air masses are very sensitive to the environment in which the stratocumuli form, and to the rate at which the stratocumuli precipitate ice. Clouds that form in moist environments and produce light ice precipitation exert a large radiative forcing on the surface. Conversely, clouds that form in dry environments or produce heavy ice precipitation are more likely to dissipate (or nearly dissipate) and exert a small radiative forcing on the surface. Arctic stratocumuli that form in less statically stable environments are also more likely to dissipate and exert a small radiative forcing. These sensitivities emphasize the importance of building general circulation model parameterizations of Arctic stratocumuli around interactions between radiative cooling, entrainment, and ice precipitation, which govern the layers' formation, persistence, and dissipation.

More broadly, the single column model simulations provide insight into the dissipation of Arctic stratocumuli and into the formation of could-top water vapor mixing ratio inversions. The simulations show that entrainment is ineffective in driving dissipation because of a stabilizing feedback between radiative cooling and the entrainment rates. In addition, the single column model simulations suggest that cloud-top vapor mixing ratio inversions may form naturally through the formation of Arctic stratocumuli in moist environments.

In the future, it would be useful to test these findings with more sophisticated numerical models, which include more accurate parameterizations for liquid and ice microphysics, and are better able to resolve processes in stratocumuli with low LWPs. In addition, it would be useful to test the sensitivity of the formation process to the background vertical velocity. Arctic stratocumuli that form in advecting air masses are also likely to form in periods of synoptic-scale lifting, and the effects of this lifting on the formation process were not investigated in this study. Finally, it would be useful to test the formation process' sensitivity to the cloud droplet number concentration. Garrett et al. (2009) found anthropogenic pollution could warm the Arctic climate by accelerating the development of Arctic stratocumuli. It is also possible that anthropogenic pollution could influence the Arctic climate through effects on cloud layers' sensitivities to the relative humidity above and below.

References

Bechtold, P., Pinty, J. P., & Fravalo, C. (1992). A model of marine boundary-layer cloudiness for mesoscale applications. *Journal of the Atmospheric Sciences*, *49*(18), 1723–1744. https://doi.org/10.1175/1520-0469(1992)049<1723:AMOMBL>2.0.CO;2

Caldwell, P., & Bretherton, C. S. (2009). Response of a subtropical stratocumulus-capped mixed layer to climate and aerosol changes. *Journal of Climate*, *22*(1), 20–38. https://doi.org/10.1175/2008JCLI1967.1

Cohen, J., Screen, J. A., Furtado, J. C., Barlow, M., Whittleston, D., Coumou, D., et al. (2014). Recent Arctic amplification and extreme mid-latitude weather. *Nature Geoscience*, *7*(9), 627–637. https://doi.org/10.1038/ngeo2234

Cronin, T. W., & Tziperman, E. (2015). Low clouds suppress Arctic air formation and amplify high-latitude continental winter warming. *Proceedings of the National Academy of Sciences*, *112*(37), 11490–11495. https://doi.org/10.1073/pnas.1510937112

Cronin, T. W., Li, H., & Tziperman, E. (2017). Suppression of Arctic air formation with climate warming: investigation with a two-dimensional cloud-resolving model. *Journal of the Atmospheric Sciences*, *74*(9), 2717–2736. https://doi.org/10.1175/JAS-D-16-0193.1

Curry, J. (1983). On the formation of continental polar air. *Journal of the Atmospheric Sciences*, *40*(9), 2278–2292. https://doi.org/10.1175/1520-0469(1983)040<2278:OTFOCP>2.0.CO;2

Curry, J. A. (1995). Interactions among aerosols, clouds, and climate of the Arctic Ocean. *Science of The Total Environment*, *160–161*, 777–791. https://doi.org/10.1016/0048-9697(95)04411-S

Curry, J. A., Ebert, E. E., & Herman, G. F. (1988). Mean and turbulence structure of the summertime Arctic cloudy boundary layer. *Quarterly Journal of the Royal Meteorological Society*, *114*(481), 715–746. https://doi.org/10.1002/qj.49711448109

Devasthale, A., Sedlar, J., & Tjernström, M. (2011). Characteristics of water-vapour inversions observed over the Arctic by Atmospheric Infrared Sounder (AIRS) and radiosondes. *Atmospheric Chemistry and Physics*, *11*(18), 9813–9823. https://doi.org/10.5194/acp-11-9813-2011

Fridlind, A. M., van Diedenhoven, B., Ackerman, A. S., Avramov, A., Mrowiec, A., Morrison, H., et al. (2012). A FIRE-ACE/SHEBA case study of mixed-phase Arctic boundary layer clouds: entrainment rate limitations on rapid primary ice nucleation processes. *Journal of the Atmospheric Sciences*, *69*(1), 365–389. https://doi.org/10.1175/JAS-D-11-052.1

Garrett, T. J., Maestas, M. M., Krueger, S. K., & Schmidt, C. T. (2009). Acceleration by aerosol of a radiative-thermodynamic cloud feedback influencing Arctic surface warming. *Geophysical Research Letters*, *36*(19). https://doi.org/10.1029/2009GL040195

Golaz, J.-C. (1997, December 5). *Development of a single-column model for simulating precipitating stratocumulus clouds* (Thesis). Colorado State University.

Gong, T., Feldstein, S., & Lee, S. (2017). The role of downward infrared radiation in the recent Arctic winter warming trend. *Journal of Climate*, *30*(13), 4937–4949. https://doi.org/10.1175/JCLI-D-16-0180.1

Harrington, J. Y. (1997, December). *The effects of radiative and microphysical processes on simulated warm and transition season Arctic stratus* (Dissertation). Colorado State University.

Harrington, J. Y., & Olsson, P. Q. (2001). On the potential influence of ice nuclei on surface-forced marine stratocumulus cloud dynamics. *Journal of Geophysical Research: Atmospheres*, *106*(D21), 27473–27484. https://doi.org/10.1029/2000JD000236

Harrington, J. Y., Sulia, K., & Morrison, H. (2013). A method for adaptive habit prediction in bulk microphysical models. Part I: Theoretical development. *Journal of the Atmospheric Sciences*, *70*(2), 349–364. https://doi.org/10.1175/JAS-D-12-040.1

Herman, G., & Goody, R. (1976). Formation and persistence of summertime Arctic stratus clouds. *Journal of the Atmospheric Sciences*, *33*(8), 1537–1553. https://doi.org/10.1175/1520-0469(1976)033<1537:FAPOSA>2.0.CO;2

Houze, R. A. (2014). *Cloud dynamics*. Oxford, England: Academic Press.

Intrieri, J. M., Fairall, C. W., Shupe, M. D., Persson, P. O. G., Andreas, E. L., Guest, P. S., & Moritz, R. E. (2002). An annual cycle of Arctic surface cloud forcing at SHEBA. *Journal of Geophysical Research*, *107*(C10). https://doi.org/10.1029/2000JC000439

Klein, S. A., McCoy, R. B., Morrison, H., Ackerman, A. S., Avramov, A., Boer, G. de, et al. (2009). Intercomparison of model simulations of mixed-phase clouds observed during the ARM Mixed-Phase Arctic Cloud Experiment. I: single-layer cloud. *Quarterly Journal of the Royal Meteorological Society*, *135*(641), 979–1002. https://doi.org/10.1002/qj.416

Langland, R. H., & Liou, C.-S. (1996). Implementation of an E-ϵ parameterization of vertical subgrid-scale mixing in a regional model. *Monthly Weather Review*, *124*(5), 905–918. https://doi.org/10.1175/1520-0493(1996)124<0905:IOAPOV>2.0.CO;2

Larsen, J. N. , O . A. Anisimov, A . Constable, A . B. Hollowed, N . Maynard, P . Prestrud, T . D. Prowse, and J.M.R. Stone, 2014: Polar regions. In: *Climate Change 2014: Impacts, Adaptation, and Vulnerability. Part B: Regional Aspects. Contribution of Working Group II to the Fifth Assessment Report of the Intergovernmental Panel on Climate Change* [Barros, V.R., C. B. Field, D.J. Dokken, M.D. Mastrandrea, K.J. Mach, T.E. Bilir, M. Chatterjee, K.L. Ebi, Y.O. Estrada, R.C. Genova, B. Girma, E.S. Kissel, A.N. Levy , S. MacCracken, P.R. Mastrandrea, and L.L. White (eds.)]. Cambridge University Press, Cambridge, United Kinggdom and New York, NY, USA, pp. 1567 - 1612 .

Lee, S., Gong, T., Feldstein, S. B., Screen, J. A., & Simmonds, I. (2017). Revisiting the cause of the 1989-2009 Arctic surface warming using the surface energy budget: downward

infrared radiation dominates the surface fluxes. *Geophysical Research Letters*, *44*(20), 10,654-10,661. https://doi.org/10.1002/2017GL075375

Lilly, D. K. (1968). Models of cloud-topped mixed layers under a strong inversion. *Quarterly Journal of the Royal Meteorological Society*, *94*(401), 292–309. https://doi.org/10.1002/qj.49709440106

Liu, S. (1998, March). *Numerical Modeling of Altocumulus Cloud Layers* (Dissertation). The University of Utah.

Loewe, K., Ekman, A. M. L., Paukert, M., Sedlar, J., Tjernström, M., & Hoose, C. (2017). Modelling micro- and macrophysical contributors to the dissipation of an Arctic mixed-phase cloud during the Arctic Summer Cloud Ocean Study (ASCOS). *Atmospheric Chemistry and Physics*, *17*(11), 6693–6704. https://doi.org/10.5194/acp-17-6693-2017

McInnes, K. L., & Curry, J. A. (1995). Lifecycles of summertimes Arctic stratus clouds. Presented at the Fourth Conference on Polar Meteorology and Oceanography, Dallas, Texas: American Meteorological Society.

Mlawer, E. J., & Clough, S. A. (1997). On the extension of rapid radiative transfer model to the shortwave region. In *Proceedings of the 6th Atmospheric Radiation Measurement (ARM) Science Team Meeting* (pp. 223–226). U.S. Department of Energy.

Mlawer, E. J., Taubman, S. J., Brown, P. D., Iacono, M. J., & Clough, S. A. (1997). Radiative transfer for inhomogeneous atmospheres: RRTM, a validated correlated-k model for the longwave. *Journal of Geophysical Research: Atmospheres*, *102*(D14), 16663–16682. https://doi.org/10.1029/97JD00237

Morrison, H., Shupe, M. D., Pinto, J. O., & Curry, J. A. (2005). Possible roles of ice nucleation mode and ice nuclei depletion in the extended lifetime of Arctic mixed-phase clouds. *Geophysical Research Letters*, *32*(18), n/a-n/a. https://doi.org/10.1029/2005GL023614

Morrison, H., Zuidema, P., Ackerman, A. S., Avramov, A., de Boer, G., Fan, J., et al. (2011). Intercomparison of cloud model simulations of Arctic mixed-phase boundary layer clouds observed during SHEBA/FIRE-ACE. *Journal of Advances in Modeling Earth Systems*, *3*(2), n/a-n/a. https://doi.org/10.1029/2011MS000066

Morrison, H., de Boer, G., Feingold, G., Harrington, J., Shupe, M. D., & Sulia, K. (2011). Resilience of persistent Arctic mixed-phase clouds. *Nature Geoscience*, *5*(1), 11–17. https://doi.org/10.1038/ngeo1332

Ovchinnikov, M., Ackerman, A. S., Avramov, A., Cheng, A., Fan, J., Fridlind, A. M., et al. (2014). Intercomparison of large-eddy simulations of Arctic mixed-phase clouds: Importance of ice size distribution assumptions. *Journal of Advances in Modeling Earth Systems*, *6*(1), 223–248. https://doi.org/10.1002/2013MS000282

Overland, J. E., Wang, M., Walsh, J. E., & Stroeve, J. C. (2014). Future Arctic climate changes: Adaptation and mitigation time scales. *Earth's Future*, *2*(2), 68–74. https://doi.org/10.1002/2013EF000162

Persson, P. O. G., Fairall, C. W., Andreas, E. L., Guest, P. S., & Perovich, D. K. (2002). Measurements near the Atmospheric Surface Flux Group tower at SHEBA: Near-surface conditions and surface energy budget. *Journal of Geophysical Research*, *107*(C10). https://doi.org/10.1029/2000JC000705

Pithan, F., Ackerman, A., Angevine, W. M., Hartung, K., Ickes, L., Kelley, M., et al. (2016). Select strengths and biases of models in representing the Arctic winter boundary layer over sea ice: the Larcform 1 single column model intercomparison. *Journal of Advances in Modeling Earth Systems*, *8*(3), 1345–1357. https://doi.org/10.1002/2016MS000630

Rossow, W. B., & Schiffer, R. A. (1999). Advances in understanding clouds from ISCCP. *Bulletin of the American Meteorological Society*, *80*(11), 2261–2287. https://doi.org/10.1175/1520-0477(1999)080<2261:AIUCFI>2.0.CO;2

Sedlar, J., & Tjernström, M. (2009). Stratiform cloud–inversion characterization during the Arctic melt season. *Boundary-Layer Meteorology*, *132*(3), 455–474. https://doi.org/10.1007/s10546-009-9407-1

Sedlar, J., Shupe, M. D., & Tjernström, M. (2012). On the relationship between thermodynamic structure and cloud top, and its climate significance in the Arctic. *Journal of Climate*, *25*(7), 2374–2393. https://doi.org/10.1175/JCLI-D-11-00186.1

Shaw, G. E., & Stamnes, K. (1980). Arctic haze: Perturbation of the polar radiation budget. *Annals of the New York Academy of Sciences*, *338*(1 Aerosols), 533–539. https://doi.org/10.1111/j.1749-6632.1980.tb17145.x

Shupe, M. D. (2011). Clouds at Arctic atmospheric observatories. Part II: Thermodynamic phase characteristics. *Journal of Applied Meteorology and Climatology*, *50*(3), 645–661. https://doi.org/10.1175/2010JAMC2468.1

Shupe, M. D., & Intrieri, J. M. (2004). Cloud radiative forcing of the Arctic surface: the influence of cloud properties, surface albedo, and solar zenith angle. *Journal of Climate*, *17*(3), 616–628. https://doi.org/10.1175/1520-0442(2004)017<0616:CRFOTA>2.0.CO;2

Shupe, M. D., Walden, V. P., Eloranta, E., Uttal, T., Campbell, J. R., Starkweather, S. M., & Shiobara, M. (2011). Clouds at Arctic atmospheric observatories. Part I: Occurrence and macrophysical properties. *Journal of Applied Meteorology and Climatology*, *50*(3), 626–644. https://doi.org/10.1175/2010JAMC2467.1

Shupe, M. D., Persson, P. O. G., Brooks, I. M., Tjernström, M., Sedlar, J., Mauritsen, T., et al. (2013). Cloud and boundary layer interactions over the Arctic sea ice in late summer. *Atmospheric Chemistry and Physics*, *13*(18), 9379–9399. https://doi.org/10.5194/acp-13-9379-2013

Smith, A. J., Larson, V. E., Niu, J., Kankiewicz, J. A., & Carey, L. D. (2009). Processes that generate and deplete liquid water and snow in thin midlevel mixed-phase clouds. *Journal of Geophysical Research*, *114*(D12). https://doi.org/10.1029/2008JD011531

Solomon, A., Shupe, M. D., Persson, P. O. G., & Morrison, H. (2011). Moisture and dynamical interactions maintaining decoupled Arctic mixed-phase stratocumulus in the presence of a humidity inversion. *Atmospheric Chemistry and Physics*, *11*(19), 10127–10148. https://doi.org/10.5194/acp-11-10127-2011

Solomon, A., Shupe, M. D., Persson, O., Morrison, H., Yamaguchi, T., Caldwell, P. M., & de Boer, G. (2014). The sensitivity of springtime Arctic mixed-phase stratocumulus clouds to surface-layer and cloud-top inversion-layer moisture sources. *Journal of the Atmospheric Sciences*, *71*(2), 574–595. https://doi.org/10.1175/JAS-D-13-0179.1

Sotiropoulou, G., Sedlar, J., Tjernström, M., Shupe, M. D., Brooks, I. M., & Persson, P. O. G. (2014). The thermodynamic structure of summer Arctic stratocumulus and the dynamic coupling to the surface. *Atmospheric Chemistry and Physics*, *14*(22), 12573–12592. https://doi.org/10.5194/acp-14-12573-2014

Stepanyuk, O., Räisänen, J., Sinclair, V. A., & Järvinen, H. (2017). Factors affecting atmospheric vertical motions as analyzed with a generalized omega equation and the OpenIFS model. *Tellus A: Dynamic Meteorology and Oceanography*, *69*(1), 1271563. https://doi.org/10.1080/16000870.2016.1271563

Stevens, B., Cotton, W. R., Feingold, G., & Moeng, C.-H. (1998). Large-eddy simulations of strongly precipitating, shallow, stratocumulus-topped boundary layers. *Journal of the Atmospheric Sciences*, *55*(24), 3616–3638. https://doi.org/10.1175/1520-0469(1998)055<3616:LESOSP>2.0.CO;2

Stohl, A. (2006). Characteristics of atmospheric transport into the Arctic troposphere. *Journal of Geophysical Research*, *111*(D11). https://doi.org/10.1029/2005JD006888

Stramler, K., Del Genio, A. D., & Rossow, W. B. (2011). Synoptically driven Arctic winter states. *Journal of Climate*, *24*(6), 1747–1762. https://doi.org/10.1175/2010JCLI3817.1

Stull, R. B. (2003). *An introduction to boundary layer meteorology*. Dodrecht: Kluwer Academic Publishers.

Sulia, K. J., Morrison, H., & Harrington, J. Y. (2014). Dynamical and microphysical evolution during mixed-phase cloud glaciation simulated using the bulk adaptive habit prediction model. *Journal of the Atmospheric Sciences*, *71*(11), 4158–4180. https://doi.org/10.1175/JAS-D-14-0070.1

Tjernström, M., Shupe, M. D., Brooks, I. M., Persson, P. O. G., Prytherch, J., Salisbury, D. J., et al. (2015). Warm-air advection, air mass transformation and fog causes rapid ice melt. *Geophysical Research Letters*, *42*(13), 5594–5602. https://doi.org/10.1002/2015GL064373

Valero, F. P. J., & Ackerman, T. P. (1985). *Arctic haze and the radiation balance* (No. NASA-TM-86784) (p. 30). Moffett Field, California: NASA Ames Research Center.

Verlinde, J., Rambukkange, M. P., Clothiaux, E. E., McFarquhar, G. M., & Eloranta, E. W. (2013). Arctic multilayered, mixed-phase cloud processes revealed in millimeter-wave

cloud radar Doppler spectra. *Journal of Geophysical Research: Atmospheres*, *118*(23), 13,199-13,213. https://doi.org/10.1002/2013JD020183

Walko, R. L., Cotton, W. R., Meyers, M. P., & Harrington, J. Y. (1995). New RAMS cloud microphysics parameterization part I: the single-moment scheme. *Atmospheric Research*, *38*(1–4), 29–62. https://doi.org/10.1016/0169-8095(94)00087-T

Wang, Z., & Sassen, K. (2001). Cloud type and macrophysical property retrieval using multiple remote sensors. *Journal of Applied Meteorology*, *40*(10), 1665–1682. https://doi.org/10.1175/1520-0450(2001)040<1665:CTAMPR>2.0.CO;2

Wilson, W. H. (1980). *Solar ephemeris algorithm* (No. SIO Ref. 80-13) (p. 70). La Jolla, California: Scripps Institution of Oceanography.

Wood, R. (2012). Stratocumulus clouds. *Monthly Weather Review*, *140*(8), 2373–2423. https://doi.org/10.1175/MWR-D-11-00121.1

Zhang, Q. (1999, May). *Modeling of Arctic stratus cloud formation and the maintenance of the cloudy Arcitc boundary layer* (Dissertation). University of Alaska Fairbanks.